Journal of Guidance, Control, and Dynamics
Vol. 48, No. 1, January 2025

Jacobian Spheroids, Shallow Encounters, and the Keyhole Map

Alessandro Masat*
Polytechnic University of Milan, 20156 Milan, Italy
Amedeo Rocchi† and Arnaud Boutonnet‡
European Space Operations Centre (ESA/ESOC), 64923 Darmstadt, Germany
and
Camilla Colombo§
Polytechnic University of Milan, 20156 Milan, Italy

https://doi.org/10.2514/1.G008013

The study of the dynamics of flybys is featured in several space-mission-related applications, spanning from the design of interplanetary orbits to the computation of impact probabilities with given celestial bodies in planetary protection and defense tasks. While patched-conics, two-body models suffice in accuracy for trajectory planning cases, collision probability assessment requires instead more insightful approaches. High-fidelity simulations have shown impact patterns to happen outside nominally colliding trajectories in terms of two-body analysis, all caused by distant or weak interactions between the given trajectory-celestial body pairs. This work proposes a novel concept of sphere of influence based on the Jacobian of the three-body dynamics, resulting in a wider definition of encounters that encompasses weak interactions up to an arbitrary threshold. The so-defined Jacobian spheroids are then used to construct the Keyhole map, a graphical tool that maps in the orbital elements space both nominal and off-nominal keyholes, i.e., collision paths accounting for three-body weak interactions. The proposed concepts arise from and are compared against the on-ground casualty risk assessment of the European Space Agency's mission JUICE.

I. Introduction

CLOSE encounters have played a relevant role in all interplanetary endeavors, being the enabling factor to design trajectories to any celestial body in the solar system with low fuel consumption. Example missions include, but are not limited to, the historical milestone-setters Voyager 1, Voyager 2 [1], and Cassini-Huygens [2], as well as the more recently launched Bepi-Colombo [3] and Solar Orbiter [4] to the inner solar system and JUICE [5] to the Jovian moons. Despite simple, two-body patched-conics models suffice to model gravity assists for mission analysis purposes, both in the open interplanetary space and for moon-tour operations. The pursuit of such trajectories opens a new area where the study of close encounters becomes relevant: planetary protection (PP) policies prescribe maximum values of impact probability for human-crafted objects with major bodies in the solar systems. Such policies aim at preventing the contamination of planetary environments from external sources and act on different levels of the mission preparation. Sterilization procedures are devised for landers, whereas the maximum impact probability threshold is all the remaining protection for objects, such as launcher upper stages, that cannot be sterilized [6,7]. This last aspect motivates the research of this work: as such impact probabilities must be ensured over particularly long time intervals, close encounters leading to orbital resonances and keyholes must be studied with statistical tools to account for all the possible future encounters.

At the same time, the study of flybys is also relevant for planetary defense tasks. This field gained prominence in the past two decades, when few asteroids have been detected to possibly closely approach, hence threat, Earth. For instance, the 2029 predicted passage of the asteroid Apophis [8] between Earth and moon has sparked interest in developing novel and more accurate approaches that do not limit their analysis at the current encounter, seeking instead to assess the possibility of future threatening returns. Valsecchi et al. [9–12] developed an analysis of resonant returns using the B-plane reference frame [13] (a planetocentric reference system based on Öpik's variables [14]). This visualization has been combined with a line-of-variation approach for the propagation of the initial uncertainty measurement [15–18], computing the impact probability of given asteroids with specific planets. The approach relies on two-body-related concepts, hence inevitably suffering from the limitations of this model: later works [19] showed that impacting orbits may be found also in off-nominal resonance conditions, all related to weak interactions between the propagated trajectory and the close encounter body. These cases make the B-plane theory specifically lose its foundations, giving rise to singularities in the mathematical formulation. For this reason, the complete understanding of impacting patterns requires an extended approach that encompasses encounters of all kinds.

To mitigate the just mentioned issues, most high-fidelity state-of-the-art approaches rely on Monte Carlo strategies [20–23]; however, a transition to less computationally intensive analyses remains desirable, exploiting the dynamic links between close encounters and future returns. Boutonnet and Rocchi [19] proposed a deep analysis stemming from the possible debris reentry analysis and the associated causality risk on the ground of the JUICE mission [5]. The traditional definitions of sphere of influence (SOI) and HIll's sphere are also not general enough to describe weak interactions, as Boutonnet and Rocchi observed them happening at greater distances from Earth [19]. A brief recap of their work is given in Sec. II.A.

Russell's review paper [24] provides an extensive review of the perturbing effects affecting spacecraft trajectories, with particular focus on the deviation from the Keplerian solution and highlighting techniques and applications related to trajectory and mission design. It highlights the presence of a wide range of works that characterize a family of trajectories in the circular restricted three-body problem (CR3BP) with a strong focus on trajectory design applications. Yet, to the best of the authors' knowledge, very few concepts from the CR3BP theory have been used to propose models and techniques

Received 29 October 2023; accepted for publication 4 July 2024; published online Open Access 2 September 2024.

*Ph.D. Graduate, DAER—Department of Aerospace Science and Technology, Via G. La Masa 34; currently Mission Analyst, OPS-GFA, IMS Space Consultancy GmbH for ESA-ESOC, Robert-Bosch-Str. 5, Darmstadt, Germany; alessandro.masat@ext.esa.int.

†Mission Analyst, OPS-GFA, GMV for ESA-ESOC, Robert-Bosch-Str. 5; amedeo.rocchi@ext.esa.int.

‡Senior Mission Analyst, OPS-GFA, ESA-ESOC, Robert-Bosch-Str. 5; arnaud.boutonnet@esa.int.

§Associate Professor, DAER—Department of Aerospace Science and Technology, Via G. La Masa 34; camilla.colombo@polimi.it.

for impact hazard assessment. Almost all the literature connected to this specific topic relies on intrinsically two-body models of heliocentric and flyby trajectories [9–13,15–19]. A few exceptions are represented by the Tisserand–Poincaré graph [25] and the Keplerian map [26–28]: in the latter, the near-instantaneous heliocentric trajectory variation by mapping its effects on the heliocentric Keplerian elements through Gauss's planetary equation. While these techniques are relevant steps in the direction of the three-body dynamics, their reliance on two-body-related integrals of motion to describe the observed phenomena may be the limiting factor to their establishment as three-body-proven models. The orbital elements definitely represent convenient quantities to describe orbits; however, they become unsuitable to model all the features of more complex interactions simply because of their definition being tied to two-body trajectories. Another example of a Keplerian element-relying approach is the recent work by Cavallari et al. [29], where a numerical study is used to determine the local quality of the patched-conics approximation.

Other works have instead focused their effort on the analysis of single trajectories experiencing flybys, e.g., the natural dynamics of asteroids in the solar system. In particular, Amato et al. [30] have focused on the numerical instability brought by close encounters in numerical simulations, aiming at identifying an optimal range where to switch the center of integration from heliocentric to planetocentric and vice versa. Romano [31] proposes instead a criterion for the detection of flybys based on the approximate values of the eigenvalues of the *N*-body Jacobian, following a step-size control technique proposed by Debatin et al. [32]. Most recently, Negri and Prado [33] conducted a comparative study between trajectories propagated with full *N*-body and two-body models, aiming at devising guidelines for asteroid trajectory computation and deflection design. A few results from the research introduced in this paragraph are recapped in Sec. II.C, as they provide some comparison and validation metrics to the results obtained in this work.

Following what presented in [34], this work uses Jacobian-based descriptors to bound the regions of motion where shallow encounters take place. These Jacobian spheroids are a more flexible and general definition, compared to SOI and Hill's sphere, because they intrinsically embed the dynamics in their formulation: SOI and Hill's sphere are "static" concepts, built on an approximate balance of perturbation forces and the stationary points of the CR3BP, respectively. On the other hand, Jacobian spheroids are built to account for the evolution of the trajectory and the local gradients of the whole gravitational field [34]. The Jacobian spheroid concept is then used to characterize Keyhole patterns that are nominally outside the traditional orbital resonance definition. Similarly to the Tisserand–Poincaré graph approach [25], the boundary of the Jacobian spheroid is used as a threshold to robustly split the domain, considering a two-body dynamics outside the spheroid, and the CR3BP inside. Following again the logic of the Tisserand–Poincaré graph theory [25], the interface between the Tisserand parameter and the Jacobi constant is used to switch between the two realms and is used as a parameter to construct a graphical visualization of all keyholes, both nominally resonant and apparently nonresonant, in the Keyhole map.

This paper starts with a recap of the traditional definitions of SOI, as well as pioneering numerical investigations attempting to extend the concepts thereof, in Sec. II, followed by the proposed encounter characterization with the Jacobian spheroids in Sec. III. Finally, the process and theory behind the Keyhole map are presented in Sec. IV.

II. Encounters and Sphere-of-Influence Definitions

The boundary to cross to assess whether a close encounter is happening or not is not clear per se, which inevitably becomes blurred in the case of shallow interactions. The commonly adopted frameworks do not fit perfectly well in these borderline cases, for different reasons.

The patched conics approximation simplifies the flyby problem into two distinct two-body phases and assumes a zero-radius SOI for an instantaneous flyby effect on the outer scale. In the inner part, instead, the trajectory is approximated by a hyperbolic solution of the two-body problem, and the trajectory deflection caused by the flyby is simply given by the rotation of the asymptotic velocity vectors [35] $\boldsymbol{v}_\infty^\pm$:

$$\boldsymbol{v}_\infty^\pm = \boldsymbol{v}^\pm - \boldsymbol{v}_{pl} \tag{1}$$

While in the secondary-centric frame the asymptotic velocities have equal magnitude, the rotation of $\boldsymbol{v}_\infty^-$ into $\boldsymbol{v}_\infty^+$ results, from the interplanetary viewpoint, in a net instantaneous $\Delta\boldsymbol{v}$ supplied to the outer trajectory:

$$\Delta\boldsymbol{v} = \boldsymbol{v}^+ - \boldsymbol{v}^- \tag{2}$$

This approximation may seem reasonable from the interplanetary viewpoint; nonetheless, it becomes inaccurate in cases of slow-velocity, distant, and/or prolonged interactions. These are completely neglected by the patched conics approximation, as well as the finite time it takes to perform a complete flyby.

On the contrary, the CR3BP introduces a synodic reference frame whose x axis is attached to the line that connects the two primary bodies. The dynamic model considers both bodies at the same time and in full, without neglecting either body in specific trajectory phases. The nondimensional CR3BP equations of motion written in the rotating frame are [35]

$$\begin{aligned}\ddot{x} &= 2\dot{y} + x - \frac{1-\pi_2}{\sigma^3}(x+\pi_2) - \frac{\pi_2}{\psi^3}(x-1+\pi_2)\\ \ddot{y} &= -2\dot{x} + y - \frac{1-\pi_2}{\sigma^3}y - \frac{\pi_2}{\psi^3}y\\ \ddot{z} &= -\frac{1-\pi_2}{\sigma^3}z - \frac{\pi_2}{\psi^3}z\end{aligned} \tag{3}$$

with

$$\begin{aligned}\pi_2 &= \frac{\mu_2}{\mu_1+\mu_2}\\ \psi &= \sqrt{(x-1+\pi_2)^2 + y^2 + z^2}\\ \sigma &= \sqrt{(x-1+\pi_2)^2 + y^2 + z^2}\end{aligned} \tag{4}$$

where μ_1 and μ_2 are the gravitational parameters of primary and secondary, respectively. The units are normalized such that the distance between primary and secondary and the gravitational parameter $\mu_1 + \mu_2$ are both equal to 1. This also results in a revolution period of the primary–secondary system around the barycenter that is equal to 2π. The CR3BP has a single integral of motion, the Jacobi constant C_J:

$$C_J = n^2(x^2+y^2) + 2\left(\frac{\mu_1}{r_1} + \frac{\mu_2}{r_2}\right) - (\dot{x}^2 + \dot{y}^2 + \dot{z}^2) \tag{5}$$

with r_1 and r_2 are distances from bodies 1 and 2, respectively, and n is the angular rate of the synodic frame. Far from the secondary body and with $\mu_1 \gg \mu_2$, the Jacobi constant can be approximated by the Tisserand parameter $\mathcal{T}$:

$$\mathcal{T} = \frac{1}{a} + 2\sqrt{a(1-e^2)}\cos i \approx C_J \tag{6}$$

where a is the nondimensional semimajor axis (SMA), expressed with reference length as the SMA of body 2 with respect to body 1.

Despite that the CR3BP is a more comprehensive framework than the Keplerian approximation, in some phases of the trajectory the effects of one of the two bodies could be actually neglected. In addition, the more complex dynamic model prevents the use of analytical solutions, thereby restricting possible analysis to simulation and map-based approaches.

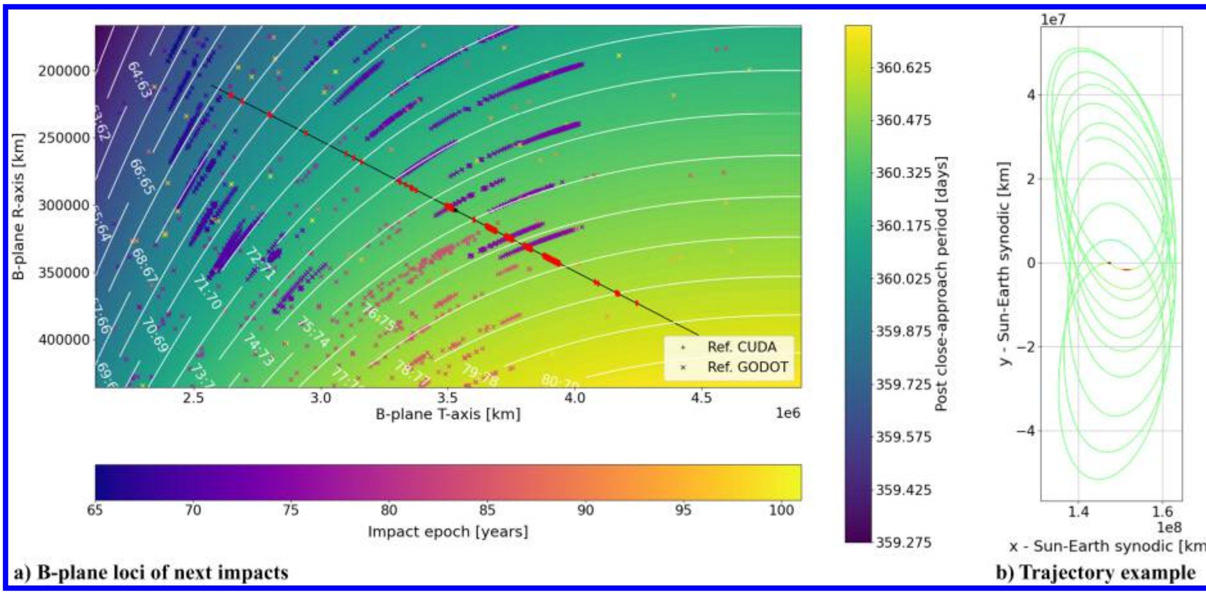

Fig. 1 Impacting (a) and diverging (b) trajectories found by Boutonnet and Rocchi [19]. Pictures from [19].

A. JUICE Space Debris Mitigation and On-Ground Casualty Risk Case

In the Earth case, not only PP requirements come into play but also ESA's Space Debris Mitigation (SDM) policies and the French Space Operations Act for missions launched from French territory (including French Guyana). In fact, similarly to PP analysis, this additional set of policies requires the assessment of impact probabilities over both short and long time intervals. For this reason, Boutonnet and Rocchi studied the taxonomy of Earth-impacting trajectories and highlighted a connection between impacts and specific regions in Earth's B-plane, all associated with three-body interactions among the propagated sample, Earth, and the Sun. In particular, Fig. 1a represents the detected impacts in the whole sampled domain as red, purple, and salmon crosses, colored according to the impact epoch. Such crosses are denoted either with $\times$ or $+$ according to the software they have been sampled with, i.e., GODOT [36] and CUDAjectory [21,37,38], respectively. The chart background color scale represents the postencounter orbital period, associated with white level curves representing the nominal orbital resonances, according to the definition by [10]. Although some impacts align with these resonance lines, Boutonnet and Rocchi found a nonnegligible amount of impacting off-resonance samples. They define a few different families of colliding trajectories with the A–E letters, which differ in their respective behavior, but all have in common the dynamics type that leads to the impact: a distant, shallow encounter introduces a slight modification in the orbital period of the propagated sample. Despite being small in magnitude, this action is large enough to make the trajectories deviate significantly from the original pattern predicted by the B-plane resonances. For instance, C-type impacts correspond to cycloids that perform a shallow encounter that increases the sample orbital period and makes them switch from a counterclockwise cycloid to a clockwise one. Thus, instead of passing over and then moving away from Earth without interactions, the deflected cycloid returns close to Earth and eventually collides, following a dynamics that the original B-plane could not predict (as the example trajectory in Fig. 1b).

Boutonnet and Rocchi [19] attempted to explain such observed interactions with traditional two-body-based concepts, such as orbital resonances being simply described by the ratio of the orbital period at a given instant in time, together with its representation as contour lines in the B-plane. Moreover, the B-plane visualization itself becomes ill-defined at great distances from a given planet and for slow encounter velocities [10,13,14,39], making it an unsuitable tool to study the problem at hand.

B. Sphere of Influence and Hill's Sphere

The two most common definitions for the boundary that splits heliocentric and planetary domains are the SOI and the Hill's sphere. Denoting the SMA of body 2 around body 1 with a_2, the former is identified by

$$r_{\mathrm{SOI}} \approx a_2 \left(\frac{\mu_2}{\mu_1}\right)^{2/5} \tag{7}$$

and stems from equaling the perturbations of the two gravitational fields. For instance, in the Sun–Earth case, the SOI approximates the distance where the gravitational perturbation of the Sun on the Earth's gravitational field equals the perturbation of the Earth on the Sun's gravitational field [35]. On a different approach, the Hill's sphere radius is defined from two of the local maxima of the CR3BP potential,¶ as the approximate distance of the Lagrange points L1 and L2 from the secondary body:

$$r_{\mathrm{Hill}} \approx a_2 \sqrt[3]{\frac{\mu_2}{3\mu_1}} \tag{8}$$

Five of these points exist and can be found as the points where the centrifugal acceleration of the synodic frame balances the combined gravitational field of both the primary and the secondary [35].

C. Numerical Investigations

The dynamics' Jacobian is traditionally linked to the step size control for numerical simulations. In particular, the maximum eigenvalue influences the stability of the numerical scheme [40]. Contrarily to predictor-corrector integrators (e.g., the Runge–Kutta family), other adaptive schemes use the knowledge of the dynamics of the of the Jacobian to minimize the truncation error at each step. In the orbital dynamics case, the work of Debatin et al. [32] used an analytical approximation of the maximum Jacobian eigenvalue of the restricted N-body dynamics, building a fast integration algorithm with step size control. In particular, the dynamics of the restricted N-body problem can be written with barycentric coordinates as

¶This potential is not purely gravitational from the small-body perspective, as it includes the rigid rotation of the primary–secondary system around its barycenter as an "external" constant contribution. Strictly speaking, the rotation of the system is indeed caused by the reciprocal gravitational effects of primary and secondary.

$$\ddot{\boldsymbol{r}} = \sum_{i=1}^{N} \boldsymbol{f}_i(\boldsymbol{r}, t) = -\sum_{i=1}^{N} \frac{\mu_i}{|\boldsymbol{d}_i(t)|^3} \boldsymbol{d}_i(t) \tag{9}$$

with $\boldsymbol{d}_i = \boldsymbol{r} - \boldsymbol{r}_i$. Introducing the velocity vector $\boldsymbol{v}$, Eq. (9) can be rewritten as a system of six first-order ordinary differential equations on the full state $\boldsymbol{x} = \{\boldsymbol{r}, \boldsymbol{v}\}$:

$$\boldsymbol{x} = \boldsymbol{f}(\boldsymbol{x}, t) = \begin{cases} \dot{\boldsymbol{r}} = \boldsymbol{v} \\ \dot{\boldsymbol{v}} = \boldsymbol{f}(\boldsymbol{r}, t) \end{cases} \tag{10}$$

The Jacobian $\boldsymbol{J}$ of the dynamics $\boldsymbol{f}(\boldsymbol{x}, t)$ is obtained computing the partial derivatives of $\boldsymbol{f}(\boldsymbol{x}, t)$ with respect to the state $\boldsymbol{x}$, as

$$\boldsymbol{J} = \frac{\partial \boldsymbol{f}}{\partial \boldsymbol{x}} = \begin{bmatrix} \boldsymbol{0} & \boldsymbol{I} \\ \boldsymbol{G} & \boldsymbol{0} \end{bmatrix} \tag{11}$$

with $\boldsymbol{0}$ and $\boldsymbol{I}$ the 3×3 null and identity matrices, respectively, and $\boldsymbol{G} \coloneqq \partial \boldsymbol{f}(\boldsymbol{r}, t)/\partial \boldsymbol{r}$, which can be explicitly written as

$$\boldsymbol{G} = \sum_{i=1}^{N} \frac{\partial \boldsymbol{f}_i}{\partial \boldsymbol{r}} = \sum_{i=1}^{N} \boldsymbol{G}_i = \sum_{i=1}^{N} \frac{\mu_i}{|\boldsymbol{d}_i|^5} \left(|\boldsymbol{d}_i|^2 \boldsymbol{I} - 3 \boldsymbol{d}_i \boldsymbol{d}_i^T \right) \tag{12}$$

Consequently, the eigenvalues ν_i of $\boldsymbol{J}$ can be computed as

$$\det \begin{bmatrix} \nu \boldsymbol{I} & -\boldsymbol{I} \\ -\boldsymbol{G} & \nu \boldsymbol{I} \end{bmatrix} = 0$$

which becomes

$$\det(\lambda \boldsymbol{I} - \boldsymbol{G}) = 0$$

with $\lambda = \nu^2$, for the properties of the determinant of block-square matrices [41]. Coincidentally, the original sixth-order characteristic polynomial of $\boldsymbol{J}$ has reduced to the third-order polynomial of $\boldsymbol{G}$, thereby making the Jacobian eigenvalues the complex conjugate numbers identified by $\nu_{j,j+3} \equiv \pm\sqrt{\lambda_j}$, with $j = 1, 2, 3$. In other words, the six eigenvalues $\nu_{j,j+3}$ of the Jacobian $\boldsymbol{J}$ are related to the three eigenvalues λ_j of the matrix $\boldsymbol{G}$ through a simple squaring, and considering both the plus and minus sign possibilities. Considering the submatrices $\boldsymbol{G}_i$ related to the different N bodies, analytical expressions exist for the corresponding $\lambda_j^{(i)}$:

$$\lambda_1^{(i)} = \lambda_{\max}^{(i)} = \frac{2\mu_i}{d_i^3}, \quad \lambda_2^{(i)} = \lambda_3^{(i)} = -\frac{\mu_i}{d_i^3} \tag{13}$$

Debatin et al. approximated maximum Jacobian eigenvalue $\nu_{\max}$ as the sum of the squares of all the separate two-body Jacobian eigenvalues, exploiting the relationship between the eigenvalues of $\boldsymbol{J}$ and $\boldsymbol{G}$ [32]:

$$\nu_{\max} \approx \sqrt{\sum_{i=1}^{N} \nu_{\max}^{(i)2}} = \sqrt{\sum_{i=1}^{N} \lambda_{\max}^{(i)}} \tag{14}$$

with the superscript i denoting the ith body. This approximation becomes particularly reliable far from the boundaries of any SOI/Hill's sphere, since in these regions either the Sun or the planet flown by heavily dominates the dynamics.

The later work of Romano [31] used a similar approximation approach to implement a flyby detection criterion. In particular, in the event of the ratio between the eigenvalues of a given planet and the Sun growing above a user-specified tolerance, a flyby event would be detected:

$$\frac{\lambda^{(i)}}{\lambda^{(\mathrm{Sun})}} \geq \mathrm{tol}, \quad \text{with } i = 1, \ldots, N \tag{15}$$

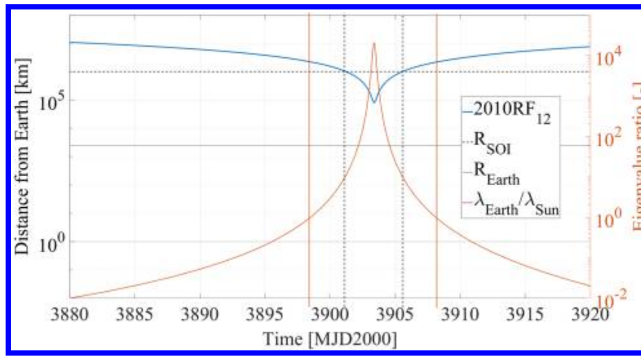

Fig. 2 Distance from Earth and eigenvalue ratio evolution for the asteroid 2010RF$_{12}$ in the Sun–Earth case.

Romano also showed that this criterion encompasses the usually defined SOI/Hill's sphere: in the case of his arbitrary choice of setting the threshold equal to 1, the critical ratio is triggered at greater distances from the secondary body, compared to SOI and Hill's sphere. Figure 2 provides an example with the evolution of the eigenvalue ratio for the 2010RF$_{12}$ in the Sun–Earth case. The left y axis provides a scale of the distance from Earth, whereas the right y axis presents the corresponding values of the Earth-to-Sun eigenvalue ratio. The x axis shows the epochs associated with 2010RF$_{12}$'s Earth close approach instead. The eigenvalue ratio equals 1 at greater distances from Earth (red lines) compared to the SOI case (black dashed lines), resulting in a wider definition of SOI and, therefore, of encounter.

The work of Amato et al. [30] reached a similar conclusion to what observed in [31]: in particular, they identify the best distance to switch the center of integration, moving from heliocentric to planetocentric orbital propagation and vice versa, in terms of numerical stability of the propagation, in the area encompassed by approximately one to three Hill's radii. This suggests that this distance range may have a particular dynamic meaning, also representing a useful numerical and experimental reference to compare against.

Most recently, Cavallari et al. [29] studied the case of Earth's SOI searching for a suitable size while also accounting for velocity-related three-body effects on the dynamics, proposing an optimization-based approach that results in different SOI radii depending on the initial conditions, according to the local quality of the patched conics approximation when compared to the CR3BP. The definition of a radii database is also included, which can be used with interpolation techniques to generalize the results for other, nontested initial states. Cavallari et al. [29] find that the identified radii all fall within the optimal switch range proposed by Amato et al. [30].

The latest work by [33] presents a detailed numerical survey of the effect of shallow encounters on asteroid deflection predictions and trajectory design. In particular, they assess the accuracy of a simple analytical model on the overall postshallow encounter predicted trajectory. Ultimately, they devise guidelines for the use of such analytical models, identifying the threshold of 15 times the Hill's radius as a conservative limit for the reliability of analytical two-body techniques, outside of which the effects of the corresponding bodies can be safely neglected. This work highlights the complexity of encounters, numerically demonstrating that the traditional SOI and Hill's spheres are not suited for the accurate characterization of encounters.

III. Dynamic Flyby Characterization: Jacobian Eigenvalues

A method to bridge the gap between the patched conics and the CR3BP realms for the study of close encounters is presented, aiming at identifying a new and robust criterion for the definition of the SOI of a planet. Such a criterion should make a more general framework compared to the traditional SOI and Hill's sphere definitions, possibly allowing the study of shallow and distant interactions.

A. Dynamic Analysis: Keplerian Error, Local Lyapunov Exponents, and Jacobian Eigenvalues

Considering the generic restricted three-body problem (R3BP), the function $\boldsymbol{f}(\boldsymbol{r}, t)$ in the dynamic system presented in Eq. (10) reduces to $\boldsymbol{f} = \boldsymbol{f}_1 + \boldsymbol{f}_2$, associated to the bodies 1 and 2. Assuming $\mu_1 > \mu_2$, bodies 1 and 2 can be labeled as the *primary* and the *secondary,* respectively. A graphical representation of this geometric configuration is given in Fig. 3. With the goal of studying the local relative influence of each body on the dynamics around a reference state $\tilde{\boldsymbol{x}}$, the R3BP dynamic system of Eq. (10) can be linearized, leading to

$$\Delta\dot{\boldsymbol{x}} = \boldsymbol{J}|_{x=\tilde{x}}\Delta\boldsymbol{x} \tag{16}$$

with $\boldsymbol{J}, \boldsymbol{G}$ that follows the definitions given in Eqs. (11) and (12) for $N = 2$, and $\Delta\boldsymbol{x} = \{\Delta\boldsymbol{r}, \Delta\boldsymbol{v}\} = \boldsymbol{x} - \tilde{\boldsymbol{x}}$. In particular, the two approximations $\boldsymbol{f} \approx \boldsymbol{f}_i$ with $i = 1, 2$, can be compared against the full dynamics function $\boldsymbol{f}$ at $\tilde{\boldsymbol{x}}$, using the corresponding linearized approximations. In addition, since the gravitational dynamics result in acceleration contributions only (without velocity kicks), the analysis can be reduced to the acceleration-related components only:

$$\Delta\dot{\boldsymbol{v}}_i = \boldsymbol{G}_i|_{r=\tilde{r}}\Delta\boldsymbol{r}_i \tag{17}$$

Equation (17) represents the local effect of the corresponding Keplerian dynamics over small perturbations to the reference state $\tilde{\boldsymbol{x}}$. The subscript i highlights that the considered subsystem is the corresponding Keplerian linear approximation, i.e., considering only body i. Linear systems theory uses the eigenvalues of the system matrix evaluated on an equilibrium point to define the stability of such equilibrium. In the Keplerian dynamics case, equilibria would appear at infinite distance, and hence the Jacobian eigenvalues cannot be interpreted as the traditional stability metric. Nonetheless, Jacobian eigenvalues can always be interpreted as *local Lyapunov exponents* [42,43]: they always represent a measure of the local predictability of the system, which increases for decreasing values of the Lyapunov exponents. While the eigenvalue expressions given in Eq. (13) reveal that any chosen noninfinitely distant point always features the maximum eigenvalue $\lambda_1 > 0$ (i.e., also $\nu_1 > 0$), the presence of analytical solutions to the Kepler problem mitigates the related unpredictability of the system. In other words, while small perturbations effectively make two close solutions diverge, the two trajectories can still be computed analytically. Differently, the transition to the three-body problem results in too few integrals of motion to obtain analytical solutions, resulting in a persistently chaotic and unpredictable system: observing that in any point of the domain $\mathrm{Trace}(\boldsymbol{G}_i) \equiv 0$, then the maximum eigenvalue of $\boldsymbol{G} = \boldsymbol{G}_1 + \boldsymbol{G}_2$ will always be larger than or equal to zero. Despite equilibrium points (the Lagrange points) that can be found in the context of the CR3BP, the objective of this study is to quantify the dominance of primary and secondary across the state space. For this reason, no implicit assumption about the existence of equilibria is made, building a local but generic characterization of the separate two-body dynamics comparing them to each other and to the complete R3BP.

Recalling that $\boldsymbol{G} \equiv \boldsymbol{G}_1 + \boldsymbol{G}_2$ in the R3BP, the matrix approximation error $\Delta\boldsymbol{G}_i$ of $\boldsymbol{G} \approx \boldsymbol{G}_i$ is directly defined as $\Delta\boldsymbol{G}_i \equiv \boldsymbol{G}_k$, with $i, k = 1, 2$ and $i \neq k$. From this observation, the Keplerian linearized error $\Delta\mathbf{ex}_i$ can be defined as

$$\Delta\mathbf{ex}_i = \begin{cases} \Delta\mathbf{er}_i = \Delta\boldsymbol{r} - \Delta\boldsymbol{r}_i \\ \Delta\mathbf{ev}_i = \Delta\boldsymbol{v} - \Delta\boldsymbol{r}_i \end{cases} \tag{18}$$

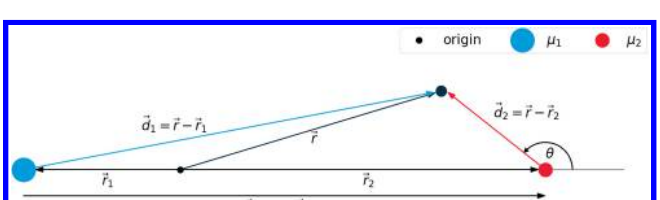

Fig. 3 Geometrical configuration of the considered R3BP.

and the following error system can be built:

$$\begin{cases} \Delta\dot{\mathbf{er}}_i = \Delta\mathbf{ev}_i \\ \Delta\dot{\mathbf{ev}}_i = \Delta\boldsymbol{G}_i|_{r=\tilde{r}}\Delta\mathbf{er}_i \end{cases} \tag{19}$$

which rearranged in matrix form becomes

$$\Delta\dot{\mathbf{ex}}_i = \Delta\boldsymbol{J}_i|_{x=\tilde{x}}\Delta\mathbf{ex}_i \equiv \boldsymbol{J}_k|_{x=\tilde{x}}\Delta\mathbf{ex}_i, \quad i, k = 1, 2 \quad \text{and} \quad i \neq k \tag{20}$$

In other words, the Keplerian variational equations for body k locally model the evolution of the error made by the approximation $\boldsymbol{f} \approx \boldsymbol{f}_i$, with $i, k = 1, 2$ and $i \neq k$. Reducing once again the study to the error matrix $\Delta\boldsymbol{G}_i \equiv \boldsymbol{G}_k$, the chosen metric can be condensed to its Euclidean norm $|\boldsymbol{G}_k|_2$. Since $\boldsymbol{G}_k$ is symmetric, as Eq. (12) highlights, its Euclidean norm corresponds to its maximum eigenvalue, whose absolute value is also called *spectral radius* $\rho(\boldsymbol{G}_k)$:

$$|\Delta\boldsymbol{G}_i|_2 \equiv |\boldsymbol{G}_k|_2 \equiv \rho(\boldsymbol{G}_k) \equiv \lambda_{\max}^{(k)}$$

In summary, tracking the value of the maximum two-body Jacobian eigenvalues of the reference R3BP provides a direct measure of the error made by both two-body approximations. At the same time, the local Lyapunov exponent interpretation of the Jacobian eigenvalue of the error system of Eq. (19) gives an indication of the predictability of the error system: the lower its value, the more predictable and the less diverging the error with respect to the corresponding** Keplerian approximation.

Following the just mentioned considerations, the relative "dominance" of each body over the full R3BP problem can be studied by connecting the two error systems, for body 1 and body 2, in a single figure of merit. In particular, the domain can be characterized by quantifying the error made by the best local approximation, between $\boldsymbol{G} \approx \boldsymbol{G}_1$ and $\boldsymbol{G} \approx \boldsymbol{G}_2$. This can be represented by the Jacobian Error function E_J, defined as

$$E_J = \min\left[\frac{\rho(\Delta\boldsymbol{G}_1)}{\rho(\boldsymbol{G})}, \frac{\rho(\Delta\boldsymbol{G}_2)}{\rho(\boldsymbol{G})}\right] \tag{21}$$

where $\rho(\boldsymbol{G})$ simply serves to present the local error in relative terms. The body that provides the minimum error contribution to the min() function can be said to locally dominate the dynamics. Figure 4 shows the values taken by E_J in the planar Sun–Earth case, representing the values taken by E_J in the logarithmic color scale and comparing it against the definitions of SOI (dotted black), Hill's sphere (dashed black), and the 3× and 15× multiples of the Hill radius, as such values have been mentioned in [30] and [33], respectively. In particular, the region identified by 1× to 3× Hill's radii bounds the domain region where $E_J \geq 10^{-1}$, as it can be seen in Fig. 4b. Looking instead at Fig. 4a, the 15× range represents a conservative threshold for regions where $E_J \geq 10^{-3}$. The axes reference unit is the astronomical unit [au].

As it could be intuitively expected, the proposed metric based on the Jacobian error E_J highlights a smooth transition between regions heavily dominated by the Sun, passing through regions where this dominance becomes weaker, arriving to the SOI range where Earth is the dominant body instead. This also explains why the obtained characterization is continuous, despite the min() function could, in general, introduce discontinuities. Interestingly, Fig. 4a highlights an eccentricity of the different levels of E_J with respect to the symmetry associated with the SOI and Hill's sphere definitions that becomes increasingly visible for increasing distances from Earth. In addition, Fig. 4b shows regions of increased E_J close to the maximum error area, approximately perpendicular to the Sun–Earth line but slightly skewed toward the Sun. For these reasons, while the presented results

**The error system characterized by $\boldsymbol{G}_k$ corresponds to the Keplerian approximation $\boldsymbol{G} \approx \boldsymbol{G}_i$, with $i, k = 1, 2$ and $i \neq k$.

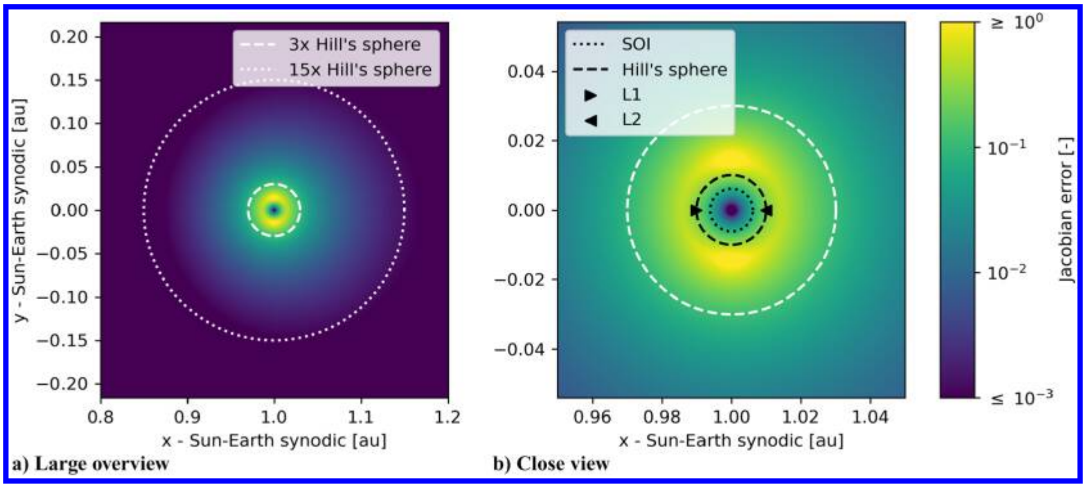

Fig. 4 Jacobian error function for the Sun–Earth case.

are connected to the 3× and 15× threshold found in [30,33], the link could be due to the small values of μ_{Earth} relative to μ_{Sun}. Such considerations can be expected to still match for μ_2/μ_1 ratios close to the Earth–Sun case, although different results may be observed, especially for larger values of μ_2, e.g., for the Jupiter–Sun case. A possible physical interpretation of the observed results and of this consideration is given in Sec. III.B.

B. Hamiltonian Interpretation and Gravitational Potential Curvature

Position and velocity vectors $\boldsymbol{r}$ and $\boldsymbol{v}$ are a set of canonical variables, as they are a pair of coordinates ($\boldsymbol{r}$) and their respective conjugate momenta ($\boldsymbol{v}$) that satisfy the Poisson bracket relations:

$$\{r_i, r_j\} = 0, \quad \{v_i, v_j\} = 0, \quad \{r_i, v_j\} = \delta_{ij} \tag{22}$$

where δ_{ij} is the Kronecker delta, i.e., $\delta_{i,j} = 0$ if $i \neq j$ and $\delta_{i,j} = 1$ if $i = j$, and $\{f, g\}$ stands for the Poisson bracket operator applied to the generic functions $f = f(\boldsymbol{r}, \boldsymbol{v})$ and $g = g(\boldsymbol{r}, \boldsymbol{v})$:

$$\{f, g\} = \sum_{i=1}^{M} \left(\frac{\partial f}{\partial r_i} \frac{\partial g}{\partial v_i} - \frac{\partial f}{\partial v_i} \frac{\partial g}{\partial r_i} \right) \tag{23}$$

with M the number of coordinates $\boldsymbol{r}$, i.e., $M = 3$ in the Cartesian case. Because of the just mentioned observations, the R3BP equations of motion can be obtained from its Hamiltonian $\mathcal{H} = \mathcal{H}(\boldsymbol{r}, \boldsymbol{v}, t)$, which correspond to the total energy of the small body at the given state $\boldsymbol{x} = \{\boldsymbol{r}, \boldsymbol{v}\}$ and time t.[††] $\mathcal{H}$ can be simply defined as the sum of the kinetic energy of the small body $\mathcal{K}$ and its gravitational potential $\mathcal{V}$:

$$\mathcal{H} = \mathcal{K} + \mathcal{V} \tag{24}$$

where

$$\mathcal{K} = \frac{1}{2} \boldsymbol{v} \cdot \boldsymbol{v}, \quad \mathcal{V} = -\frac{\mu_1}{|\boldsymbol{d}_1|} - \frac{\mu_2}{|\boldsymbol{d}_2|} \tag{25}$$

Consequently, the equations of motion can be derived directly from $\mathcal{H}$ through Hamilton's equation:

$$\begin{cases} \dot{\boldsymbol{r}} = \partial\mathcal{H}/\partial\boldsymbol{v} = \partial\mathcal{K}/\partial\boldsymbol{v} = \boldsymbol{v} \\ \dot{\boldsymbol{v}} = -\partial\mathcal{H}/\partial\boldsymbol{r} = -\partial\mathcal{V}/\partial\boldsymbol{r} = \boldsymbol{f} \end{cases} \tag{26}$$

where $\boldsymbol{f} = \boldsymbol{f}(\boldsymbol{r}, t) = \boldsymbol{f}_1(\boldsymbol{r}, t) + \boldsymbol{f}_2(\boldsymbol{r}, t)$, with $\boldsymbol{f}_1$ and $\boldsymbol{f}_2$ defined as in Eq. (9). Alternatively, Eq. (26) can be written in terms of the full Cartesian state $\boldsymbol{x}$ as

$$\dot{\boldsymbol{x}} = \boldsymbol{f}(\boldsymbol{x}, t) = \boldsymbol{K} \frac{\partial \mathcal{H}}{\partial \boldsymbol{x}} \tag{27}$$

with $\boldsymbol{K}$ being

$$\boldsymbol{K} = \begin{bmatrix} \boldsymbol{0} & \boldsymbol{I} \\ -\boldsymbol{I} & \boldsymbol{0} \end{bmatrix}$$

normally called symplectic matrix.

Expressing the Jacobian $\boldsymbol{J}$ in terms of the Hamiltonian $\mathcal{H}$ gives

$$\boldsymbol{J} = \frac{\partial \boldsymbol{f}}{\partial \boldsymbol{x}} = \frac{\partial}{\partial \boldsymbol{x}} \left(\boldsymbol{K} \frac{\partial \mathcal{H}}{\partial \boldsymbol{x}} \right) = \boldsymbol{K}\, \text{Hess}(\mathcal{H}) \tag{28}$$

with Hess($\mathcal{H}$) the Hessian of the Hamiltonian. Explicitly writing Hess($\mathcal{H}$) in terms of $\mathcal{V}$ and $\mathcal{K}$ results in

$$\text{Hess}(\mathcal{H}) = \begin{bmatrix} \partial/\partial\boldsymbol{r}(\partial\mathcal{V}/\partial\boldsymbol{r}) & \boldsymbol{0} \\ \boldsymbol{0} & \partial\boldsymbol{v}/\partial\boldsymbol{v} \end{bmatrix} = \begin{bmatrix} \text{Hess}(\mathcal{V}) & \boldsymbol{0} \\ \boldsymbol{0} & \boldsymbol{I} \end{bmatrix} \tag{29}$$

Replacing the definitions of $\boldsymbol{J}$, $\boldsymbol{K}$, and Hess($\mathcal{H}$) in Eq. (28) ultimately leads to the matrix identity

$$\begin{bmatrix} \boldsymbol{0} & \boldsymbol{I} \\ \boldsymbol{G} & \boldsymbol{0} \end{bmatrix} = \begin{bmatrix} \boldsymbol{0} & \boldsymbol{I} \\ -\boldsymbol{I} & \boldsymbol{0} \end{bmatrix} \begin{bmatrix} \text{Hess}(\mathcal{V}) & \boldsymbol{0} \\ \boldsymbol{0} & \boldsymbol{I} \end{bmatrix} \tag{30}$$

from which the following link between $\boldsymbol{G}$ and $\mathcal{V}$ can be established:

$$\boldsymbol{G} \equiv -\text{Hess}(\mathcal{V}) \tag{31}$$

Hence, the Hessian of the gravitational potential $\mathcal{V}$ corresponds to the matrix $\boldsymbol{G}$ up to a change of sign of all its elements. For this reason, all the observations made for the spectral radius of $\boldsymbol{G}$ also hold for Hess($\mathcal{V}$). In other words, studying the Keplerian error through the matrices $\boldsymbol{G}_1$ and $\boldsymbol{G}_2$ corresponds to assess how much each of the two bodies is locally influencing the curvature of the whole gravitational potential. As Fig. 5 schematically shows, since $\mu_1 > \mu_2$ the potential curvature is always skewed toward μ_1, with μ_2 acting as an additional "gravitational well" in an already curved gravitational potential. Hence, since the curvature due to μ_1 decreases further from it, along the μ_1 to μ_2 line the effects of μ_2 are more prominent in a direction opposite to μ_1, explaining the observed eccentricity of the Jacobian Error E_J in Fig. 4a. Additionally, Fig. 5 also highlights a local maximum also along the μ_1 to μ_2 line, between μ_1 to μ_2 and close

[††]The R3BP is nonconservative, since the states of primary and secondary bodies are assumed to be functions of time. Nonetheless, the normal considerations made for Hamiltonian systems all hold, except for the ones assuming the conservation of energy. On the contrary, the full nonrestricted three-body problem is a conservative system. More in general, the nonrestricted N-body problem is a conservative system as well.

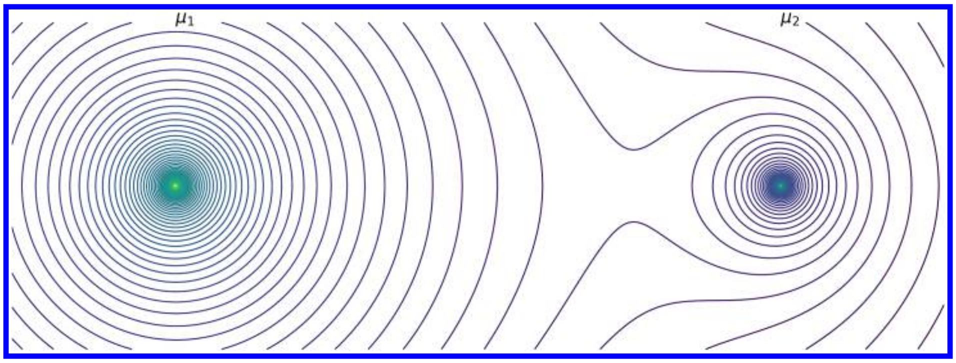

Fig. 5 Schematic magnification of the gravitational potential.

to μ_2. This can give an intuitive explanation for the higher E_J regions of Fig. 4b, that are near-perpendicular to the μ_1 to μ_2 line but slightly skewed toward μ_1. In particular, the superposed effects of the two bodies on the local curvature become relevant, with both Keplerian approximations becoming less reliable here, compared to other domain regions.

To conclude the proposed Hamiltonian analysis, the eigenvalues of Hess($\mathcal{H}$) are studied in more detail and compared to the results obtained for the eigenvalues of $\boldsymbol{J}$. Hess($\mathcal{H}$) can be rewritten as

$$\mathrm{Hess}(\mathcal{H}) = \begin{bmatrix} -\boldsymbol{G} & \boldsymbol{0} \\ \boldsymbol{0} & \boldsymbol{I} \end{bmatrix} \tag{32}$$

leading to the following characteristic equation:

$$\det\begin{bmatrix} -\boldsymbol{G} - \nu \boldsymbol{I} & \boldsymbol{0} \\ \boldsymbol{0} & (1-\nu)\boldsymbol{I} \end{bmatrix} = 0 \tag{33}$$

Once again, the properties of block square matrices [41] make Eq. (32) become

$$\det[(-\boldsymbol{G} - \nu \boldsymbol{I})((1-\nu)\boldsymbol{I})] = 0$$

In particular, a single eigenvalue is associated to $\mathcal{K}$ and is equal to 1, with multiplicity 3. The remaining eigenvalues correspond to the eigenvalues of $\boldsymbol{G}$, with a simple change of sign. Denoting with the superscripts ($\boldsymbol{J}$) and ($\boldsymbol{H}$) the eigenvalues related to $\boldsymbol{J}$ and Hess($\mathcal{H}$), respectively, the obtained results can be summarized as

$$\begin{cases} \nu_{1,4}^{(\boldsymbol{J})} = \pm\sqrt{\lambda_1} \\ \nu_{2,3,5,6}^{(\boldsymbol{J})} = \pm\sqrt{\lambda_{2,3}} \end{cases} \qquad \begin{cases} \nu_1^{(\boldsymbol{H})} = -\lambda_1 \\ \nu_{2,3}^{(\boldsymbol{H})} = -\lambda_{2,3} \\ \nu_{4,5,6}^{(\boldsymbol{H})} = 1 \end{cases}$$

with λ still denoting the eigenvalues of $\boldsymbol{G}$. In conclusion, studying the regions of relative dominance of primary and secondary in the R3BP through the matrix $\boldsymbol{G}$ and its subcomponents $\boldsymbol{G}_1$, $\boldsymbol{G}_2$ has two interconnected physical meanings. On one hand, they give a local measure of the error made by approximating the dynamics with the separate two-body cases. On the other hand, they characterize the domain using the curvature of the gravitational potential, which represents a reliable approximation of local changes in the full dynamics. Condensing this matrix-based metric with its Euclidean norm (i.e., its spectral radius) attaches the meaning of predictability of the error made by both Keplerian approximations when focusing on the Jacobian $\boldsymbol{J}$, through the local Lyapunov exponent interpretation. At the same time, as $\boldsymbol{G} \equiv -\mathrm{Hess}(\mathcal{V})$, its spectral radius represents the local maximum curvature of the gravitational potential $\mathcal{V}$, i.e., also how well the two Keplerian simplifications $\boldsymbol{G} \approx \boldsymbol{G}_1$ and $\boldsymbol{G} \approx \boldsymbol{G}_2$ can approximate it.

Interestingly, the velocity of the small body does not have any influence on the proposed characterization, despite no assumption having been made about neglecting such effects. This can be explained by having only considered the R3BP, i.e., neglecting the effects that the small body has on primary and secondary. Additionally, the positions of primary and secondary have always been considered as generic functions of time, meaning that the obtained results and characterization hold locally, at any given time t for given positions of primary and secondary $\boldsymbol{r}_1$ and $\boldsymbol{r}_2$. Intuitively, the proposed metric characterizes the domain, identifying how each body locally dominates the dynamics and how well the two Keplerian approximations can be expected to approximate the full R3BP case. For individual small-body trajectory cases, the velocity does play a relevant role in determining how much time the small body possibly spends in the different domain regions. As a final remark, the proposed analysis underlines how the transition among regions of different dominance is continuous: where to place a hard boundary to define a suitable SOI remains an arbitrary choice that, in principle, should be evaluated on a case-by-case basis, according to the accuracy requirements of the considered small-body trajectory.

C. Analytical Spheroidal Locus of Points

Figure 4 highlights a fair degree of smoothness and regularity in the observed Jacobian error function E_J [defined in Eq. (21)]. Hence, working on the definition of E_J analytical approximate solutions can be found. In particular, while the min() operator has been used as a "switch" to always select the locally best Keplerian approximation, a continuous metric is now required. Following this consideration, the two terms of the min() function in the definition of E_J can be compared by measuring their ratio and parameterizing it as γ:

$$\frac{\rho(\Delta \boldsymbol{G}_2)/\rho(\boldsymbol{G})}{\rho(\Delta \boldsymbol{G}_1)/\rho(\boldsymbol{G})} = \gamma \tag{34}$$

simplifying the term $\rho(\boldsymbol{G})$ and rewriting $\rho(\Delta \boldsymbol{G}_i)$ in terms of $\lambda_{\max}^{(k)}$, with $i, k = 1, 2$ and $i \neq k$ gives

$$\frac{\rho(\Delta \boldsymbol{G}_2)}{\rho(\Delta \boldsymbol{G}_1)} = \frac{\rho(\boldsymbol{G}_1)}{\rho(\boldsymbol{G}_2)} = \frac{\lambda_{\max}^{(1)}}{\lambda_{\max}^{(2)}} = \gamma \tag{35}$$

This expression and the flyby detection criterion proposed by [31] share many similarities, with γ playing the role of the tolerance in Eq. (15) and the only difference being an equality instead of an inequality. The physical meaning attached to the value γ can be derived from the discussions made in Secs. III.A and III.B: regions of equal γ denote loci of points where the error made by the Keplerian approximation associated with body 2 is γ times larger than the error made by the Keplerian approximation associated with body 1. Alternatively, the same loci of points can be thought of as regions where the effects of the sole body 1 on the local potential curvature are γ times stronger than the one associated with body 2. In other words, the parameter γ can be used as a gauge factor to determine which region of interest to consider, representing a direct parameter to measure the relative dominance of primary and secondary over the whole R3BP.

Figure 6 shows the values taken by γ in the Sun–Earth case, represented as colored level curves, and are compared against 1× and 3× Hill radii. The observation made about the approximate

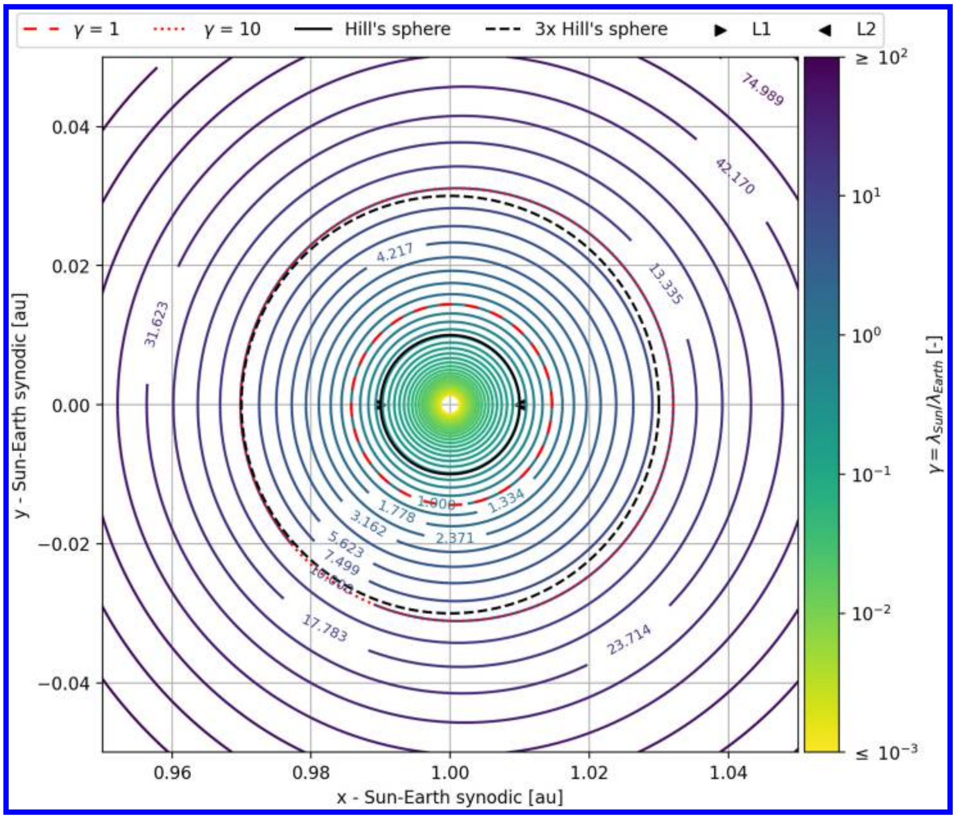

Fig. 6 Contour plot of the values of γ in the Sun–Earth case.

correspondence of the 1× to 3× Hill's radii proposed by [30] with the boundary of error higher than 10^{-1} in Fig. 4b holds: a simple change from γ to $1/\gamma$ returns exactly what previously identified, i.e., the Sun (body 1) would be taken as reference to be multiplied by the updated value $1/\gamma$ instead of the Earth (body 1), as also highlighted by the red dotted line representing $\gamma = 10$. With reference to what was discussed in Sec. III.B, the increasing eccentricity for higher values of γ matches observed in Fig. 4a can also be found in Fig. 6. Differently, the higher error regions in the proximity of the maximum error area cannot be identified by a local increase in spacing between pairs of γ level curves: this proves their meaning associated to the combined effect of both primary and secondary bodies, which is present as $\rho(\boldsymbol{G})$ in the denominators of the Jacobian error function E_J and is necessary to scale the results to suitable relative terms. In the analytical approximation, the ratio between $\lambda_{\max}^{(1)}$ and $\lambda_{\max}^{(2)}$ results in a cancellation of the term $\rho(\boldsymbol{G})$.

Continuing the search of analytical solutions, explicitly writing the definitions of $\lambda_{\max}^{(1)}$ and $\lambda_{\max}^{(2)}$ gives

$$\frac{\mu_1}{|\boldsymbol{d}_1|^3} = \gamma \frac{\mu_2}{|\boldsymbol{d}_2|^3} \tag{36}$$

and rewriting Eq. (15), expressing the position in a reference frame centered on body 2 (the secondary), results in

$$\frac{\mu_1}{|\boldsymbol{r}_2 - \boldsymbol{r}_{21}|^3} = \gamma \frac{\mu_2}{r_2^3} \tag{37}$$

where $\boldsymbol{r}_{21}$ is the position vector of body 1 with respect to body 2, as shown in Fig. 3.

Expanding $|\boldsymbol{r}_2 - \boldsymbol{r}_{21}|$ with the cosine law leads to[‡‡]

$$|\boldsymbol{r}_2 - \boldsymbol{r}_{21}| = \sqrt{r_2^2 + r_{21}^2 + 2 r_2 r_{21} \cos\theta} \tag{38}$$

[‡‡]Considering the external angle in the cosine law requires the use of the + sign.

where θ is the angle between the vectors $\boldsymbol{r}_2$ (which is equivalent to $\boldsymbol{d}_2$ because the center has been shifted on body 2) and $\boldsymbol{r}_{21}$, also shown in Fig. 3. Consequently, Eq. (37) can be rearranged as

$$\frac{r_2^2}{(r_2^2 + r_{21}^2 + 2 r_2 r_{21} \cos\theta)^2} = \left(\gamma \frac{\mu_2}{\mu_1}\right)^{2/3} \tag{39}$$

Equation (39) is quadratic on r_2, and condensing the notation with $(\gamma\mu_2/\mu_1)^{2/3} = \alpha(\gamma)$ becomes

$$(1 - \alpha(\gamma)) r_2^2 + 2\alpha(\gamma) r_{21} \cos\theta \, r_2 - \alpha(\gamma) r_{21}^2 = 0 \tag{40}$$

and can be solved analytically, provided that

$$r_2^2 + r_{21}^2 + 2 r_2 r_{21} \cos\theta \neq 0$$

Of the two $\pm$ solutions of the quadratic equations, the + family can be safely considered as the only physical one: without loss of generality,[§§] assuming that $\gamma\mu_2 < \mu_1$ makes $0 < \alpha < 1$, thereby leading to $r_2^- < 0$. Hence, the analytical solution to Eq. (40) is

$$\begin{aligned} r_2(\theta) &= \frac{\alpha(\gamma) r_{21} \cos\theta + \sqrt{\alpha(\gamma)^2 r_{21}^2 \cos^2\theta - (1-\alpha(\gamma))\alpha(\gamma) r_{21}^2}}{1-\alpha(\gamma)} \\ &= r_{21} \frac{\alpha(\gamma)\cos\theta + \sqrt{\alpha(\gamma)(1-\alpha(\gamma)\sin^2\theta)}}{1-\alpha(\gamma)} \end{aligned} \tag{41}$$

with maximum and minimum radii for $\theta = 0$ and $\theta = \pi$, respectively, given by

[§§]In case of $\alpha(\gamma) >= 1$, the gauge parameter γ could be switched to its reciprocal, with the only effect of swapping the roles of μ_1 and μ_2 as reference body. The obtained analytical solution would still be valid but would be given as centered on body 1.

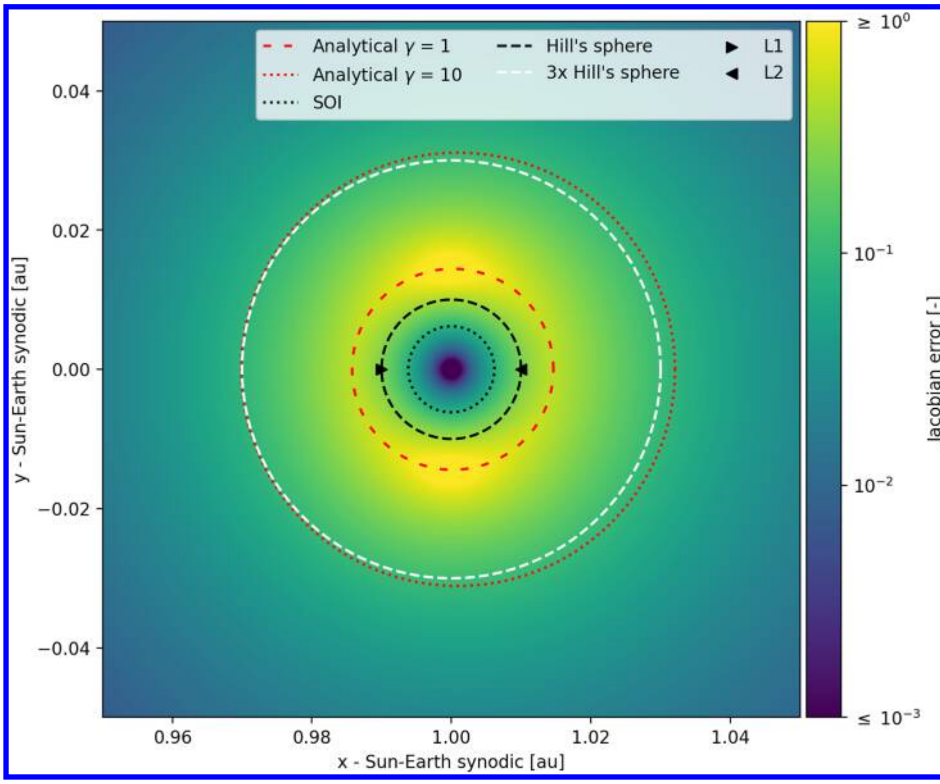

Fig. 7 Analytical solutions for $\gamma = 1{,}10$, compared against 1× and 3× radii and the Jacobian error function E_J.

$$r_2(0) = r_{21}\frac{\sqrt{\alpha(\gamma)}}{1-\sqrt{\alpha(\gamma)}}, \quad r_2(\pi) = r_{21}\frac{\sqrt{\alpha(\gamma)}}{1+\sqrt{\alpha(\gamma)}}$$

for an average radius of

$$\bar{r}_2 = r_{21}\frac{\sqrt{\alpha(\gamma)}}{1+\alpha(\gamma)}$$

Equation (41) describes a spheroidal locus of points, the *Jacobian spheroid*, axially symmetrical about the line connecting the bodies 1 and 2, as function of the distance r_{21} between the two bodies and the parameter γ. In principle, the Jacobian spheroid can be locally defined with time-varying $\boldsymbol{r}_{21}$ and angle θ in a generic R3BP. The introduction of the CR3BP would mainly result in a simplification of the evolution of $\boldsymbol{r}_{21}$. The radius of the spheroid is given as a function of θ, the angle between the test particle direction and the line connecting body 1 and body 2. Figure 7 compares two samples of the analytical solution given in Eq. (41), superposing these spheroids on what is already shown in Fig. 4b. Other than the already mentioned approximate correspondence of the $\gamma = 10$ locus (i.e., the $E_J \approx 10^{-1}$ range) with the 3× Hill's radius, it can clearly be seen that the value $\gamma = 1$ perfectly superposes with the highest observed E_J values. In conclusion, the $\gamma = 1$ line can be considered as the threshold that, once crossed, sees a switch in the locally dominating body. Nonetheless, the magnitude of this change is weak, and the effects of both bodies remain relevant in a vast domain portion around the $\gamma = 1$ line.

IV. Application: Keyhole Maps

Following the results presented in Sec. III, this section proposes to apply the PP and SDM compliance analyses. In particular, the proposed approach tries to answer the question about why many impacting trajectories in [19] happen out of nominal resonances. While Boutonnet and Rocchi [19] identify a few families for these off-nominal impacting trajectories, this section takes a step back and analyzes only the dynamics of one encounter at a time. In this first framework definition, the goal is to find and describe which parameters of the dynamics are leading to off-nominal impacting trajectories.

A. Detection of Shallow Encounters

The first step to be taken addresses a value of the spheroid parameter γ, so that the detection of shallow encounters can be arbitrarily robust. Since a link between the value of γ and possible maximum and minimum boundaries in the variation of the orbital elements has not been explored yet, an overly conservative threshold is desired, avoiding possible losses of generality due to some small, but still significant, encounter deflections being missed.

Figure 8 compares the evolution of the orbital period for one of the samples propagated in the PP analysis of the ESA Mission Solar Orbiter [4], presented in [23], with its distance from Venus, tracking the values taken by the Jacobian eigenvalues of Venus, Earth, and Jupiter.[¶¶] The orbital period is chosen for its prominent role in the identification of nominal, two-body orbital resonances, as this is the common metric used by mission analysts to characterize hazardous trajectories. Using the traditional definition of SOI would allow the detection of the two steepest variations only, without classifying some of the intermediate encounters, i.e., that indeed lead to the next deep flyby, as significant. The common x axis highlights the correspondence of the variations in the orbital period with the spikes in the eigenvalue evolution. The time steps that fall within the $\gamma = 100$ spheroid are highlighted in red in all the charts, showing that notably smaller variations of the orbital period can be detected with this approach.

Based on these considerations, the spheroid associated with $\gamma = 100$ is chosen as a boundary for two different models. Trajectories are assumed to follow a two-body heliocentric dynamics only outside this spheroid, whereas the full CR3BP is considered on the inside. While this choice is arbitrary, the numerical results shown in Fig. 8 suggest that $\gamma = 100$ is a safe enough threshold to work with. Additionally, the newly defined Jacobian spheroid is preferred over arbitrary multiples of the Hill's and SOI radii that would approximately cover the same range: the analytical Jacobian spheroids are eccentric,

[¶¶]The eigenvalue related to Jupiter is shown only as a magnitude reference.

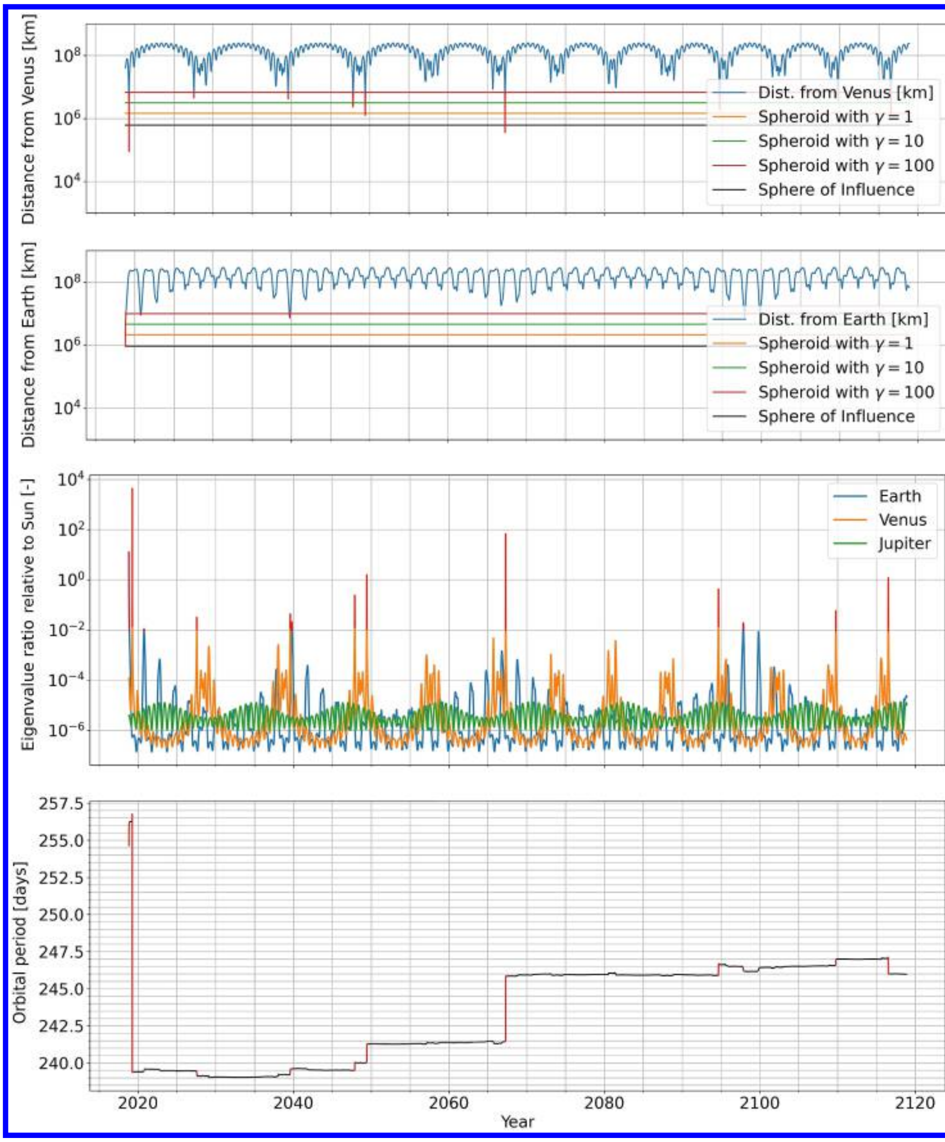

Fig. 8 Orbital period and distance from Venus and Earth. Example from the PP analysis of Solar Orbiter.

meaning that they can capture the curvature of the resulting gravitational potential in different domain regions. This results in an improved modeling of the distant interactions that can happen with similar magnitudes but at different ranges from the secondary.

B. Encounter Phasing in the Restricted Three-Body Problem

Having defined the criterion to split the domain between unperturbed two-body and CR3BP realms, a few more implications arise. Since any point of the $\gamma = 100$ spheroid boundary corresponds to a prescribed position vector, say $\boldsymbol{r}$, only three degrees of freedom (the velocity components) remain to the full determination of the orbital state at the boundary of the spheroid. Additionally, assuming the interactions to be fully ballistic and limiting the analysis to a single secondary body, the Jacobi constant C_J is conserved throughout the full integration span, thus adding a constraint between the orbit's total energy and angular momentum. Therefore, the remaining two degrees of freedom are broken down to the orbit's SMA a, tightly linked to the orbital period around body 1, and a phasing parameter, to be better identified in the following lines.

The phasing parameter should be defined based on what actually makes the trajectory become subject to an encounter. In particular, any flybys in the proposed framework are either tangent or secant to the $\gamma = 100$ spheroid boundary. Following the derivation made by Campiti et al. [44], prescribed values of SMA and Jacobi constant [in the Tisserand approximation of Eq. (6)] results, in general, in a set of four orbits passing on the same position vector $\boldsymbol{r}$: in particular, the direction of the angular momentum $\hat{\boldsymbol{h}}$ must fulfill the following conditions [44]:

$$\begin{cases} \hat{\boldsymbol{h}} \cdot \hat{\boldsymbol{k}} = \cos i \\ \hat{\boldsymbol{h}} \cdot \boldsymbol{r}_i = 0 \\ |\hat{\boldsymbol{h}}| = 1 \end{cases} \tag{42}$$

where i now identifies the inclination of the orbital plane, and $\hat{\boldsymbol{k}}$ stands for the z axis of the considered inertial reference frame. Replacing $\hat{\boldsymbol{h}} = \{\hat{h}_1, \hat{h}_2, \hat{h}_3\}$ and $\boldsymbol{r} = \{r_1, r_2, r_3\}$ gives

$$\begin{cases} \hat{h}_3 = \cos(i) \\ r_1\hat{h}_1 + r_2\hat{h}_2 + r_3\hat{h}_3 = 0 \\ \sqrt{\hat{h}_1^2 + \hat{h}_2^2 + \hat{h}_3^2} = 1 \end{cases} \tag{43}$$

and collecting the components of $\hat{\boldsymbol{h}}$ leads to [44]

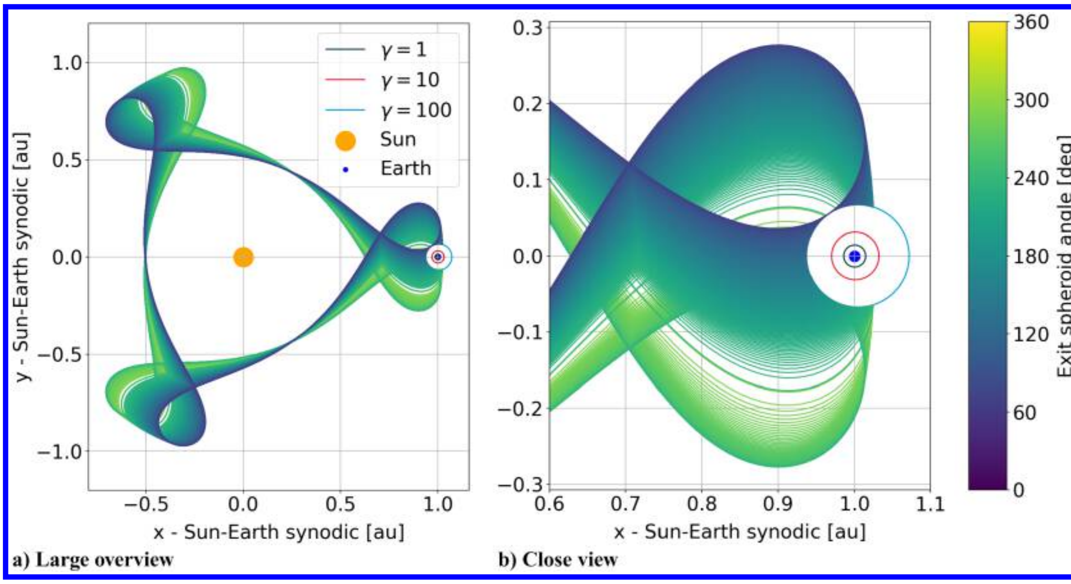

Fig. 9 Visualization of phased trajectories with the $\gamma = 100$ spheroid for $C_J = 2.95$ and the 3∶2 resonance trajectory with Earth.

$$\begin{cases} \hat{h}_3 = \cos(i) \\ \hat{h}_2 = -\dfrac{1}{r_2}\left[r_3\hat{h}_3 + r_1\hat{h}_1\right] \\ \hat{h}_1 = \pm\sqrt{1-\hat{h}_2^2-\hat{h}_3^2} = \pm\sqrt{1-\dfrac{1}{r_2^2}\left[r_3\cos(i)+r_1\hat{h}_1\right]^2-\cos(i)^2} \end{cases} \tag{44}$$

The $\pm$ in the expression for $\hat{h}_1$ highlights the existence of two possible directions of the angular momentum vector, $\hat{\boldsymbol{h}}_+$ and $\hat{\boldsymbol{h}}_-$. While $\hat{h}_3$ is fully determined by the inclination i, the remaining components of $\hat{\boldsymbol{h}}_+$ and $\hat{\boldsymbol{h}}_-$ can be obtained by numerically solving the third identity*** in Eq. (44) for $\hat{h}_{1,\pm}$. Note that $\hat{h}_{2,\pm}$ can be finally obtained from the second identity, given $\hat{h}_3$ and $\hat{h}_{1,\pm}$.

In turn, the two admissible angular momentum vectors $\hat{\boldsymbol{h}}_+$ and $\hat{\boldsymbol{h}}_-$ result in two possible directions for the line of nodes, $\hat{\boldsymbol{n}}_+$ and $\hat{\boldsymbol{n}}_-$, thereby giving two distinct values of the right ascension of the ascending node Ω_+ and Ω_- for the same inclination i. Finally, the common conics equation in polar coordinates

$$|\boldsymbol{r}| = \frac{a(1-e^2)}{1+e\cos(f)}$$

can be inverted, writing explicitly the true anomaly f. Two opposite true anomalies that correspond to the distance $|\boldsymbol{r}|$ from the primary can be computed independently of the previously obtained values of Ω_+ and Ω_-:

$$f_{1,2} = \pm\arccos\left(\frac{1}{e}\left(\frac{a(1-e^2)}{|\boldsymbol{r}|}-1\right)\right) \tag{45}$$

Additionally, two possible arguments of latitude $u_\pm$ can be obtained by the dot product $\hat{\boldsymbol{n}}_\pm \cdot \boldsymbol{r}$, which once coupled with the two true anomalies $f_{1,2}$ return four possible values of pericenter arguments $(\omega_{+,1}, \omega_{-,1}, \omega_{+,2}, \omega_{-,2})$, since $\omega = u - f$. Restricting the analysis to the planar case with inclination $i = 0$ removes the two $\pm$ cases related to the different right ascensions of the ascending node.††† The most generic solutions yield four orbits characterized by the same values of SMA a, eccentricity e, inclination i, and the four triplets $(\Omega_\pm, \omega_{\pm,1\ or\ 2}, f_{1,2})$, while only two orbits remain in the case $i = 0$, completely defined by the true anomalies f_1 and f_2. In summary, given a SMA a and a Jacobi constant C_J, any trajectory crossing or touching (the limit case with $f_1 = f_2$) the spheroid at a given point can be described simply by these two true anomaly values.

In the remaining of the section, the Sun–Earth case is considered, although the concepts could be extended to any significant pair of primary and secondary body. Figure 9 shows the different phasing of a set of heliocentric trajectories with common Jacobi constant $C_J = 2.95$ and SMA (leading to the 3∶2 resonance with Earth) in the Sun–Earth rotating frame. The phasing is described with the *exit spheroid angle* θ, the angle measured counterclockwise from the Sun-to-Earth line on the spheroid surface, shown in the color scale. The prefix "Entrance" and "Exit" for the given spheroid angle is used to stress the difference between trajectories that get inside or outside the $\gamma = 100$ spheroid, respectively, although the numerical value and the definition of the two angles are exactly the same.

Because of the prescribed Jacobi constant, not all the spheroid points result in a physical orbit, as constraints on pericenter and apocenter distances appear for a given SMA. Moreover, additional values of rotating longitude ϕ are not needed, as they would simply correspond to trajectories never being secant or tangent to the spheroid. Referring to Fig. 9, this would correspond to rigidly rotated cycloids beyond the tangent points to the spheroid, thus never experiencing any return. This means that taking the spheroid angle θ as a phasing parameter to scan upon ensures to encompass only the useful phase range to study the encounters.

Evidently, a strong link between the true anomaly f at the spheroid boundary and the spheroid angle θ exists. In particular, the *rotating longitude* ϕ can be defined as

$$\phi = \omega_{\mathrm{rot}}(t) + f \tag{46}$$

with $\omega_{\mathrm{rot}}(t)$ the *rotating* pericenter argument: in the planar case and using the Sun–Earth synodic frame, the inertial pericenter argument precesses clockwise,‡‡‡ with a rate that equals the rotation rate of the synodic frame:

$$\omega_{\mathrm{rot}} = \omega_0 - nt \tag{47}$$

***Since the argument of the square root must be positive, this constraint provides boundaries for the numerical search [44].

†††Its value becomes arbitrary and is usually set equal to 0.

‡‡‡In the nonplanar case, the angular orbital parameter featuring a clockwise precession would instead be the right ascension of the ascending node Ω, following the same precession rate of the planar case for the pericenter argument.

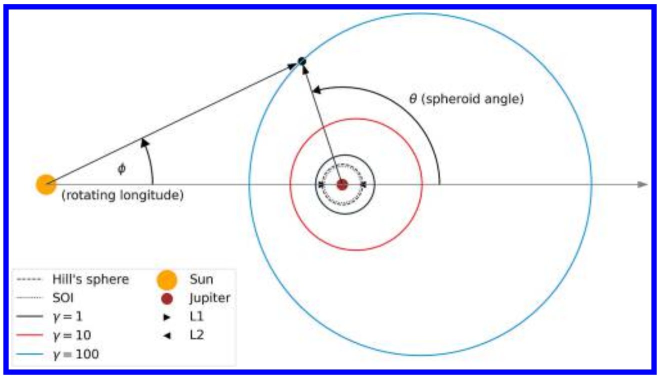

Fig. 10 Link between the spheroid angle θ and the rotating longitude $\phi = \omega_{\mathrm{rot}} + f$ in the case of Jupiter.

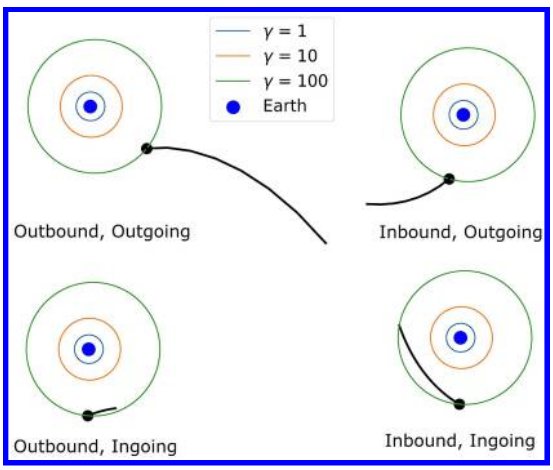

Fig. 11 Topology of spheroid-phased trajectories. Sun always on the left, toward the $-x$ direction, in all the four cases.

where n is the angular rate of the rotating frame. If ω_0 is chosen as the Sun–Earth direction at the time $t = 0$, then letting $\omega = \omega_{\mathrm{rot}}$ pairs the rotating longitude ϕ with the heliocentric orbital elements. In summary, the phasing of the orbit (i.e., the particular point of entrance/exit to/from the spheroid) is a function of the orbital parameters and the initial condition only. Figure 10 shows the link between the rotating longitude ϕ and the spheroid angle θ for the Sun–Jupiter case, as Jupiter's higher gravitational parameter allows a clearer visualization of the two angles. Nonetheless, the same considerations hold for any given pair of primary and secondary bodies. While ϕ presents ambiguous values to describe the Sun-facing and the out-facing sides of the Jacobian spheroids, the spheroid angle θ does not, thereby making it the most suitable choice as the reference phasing parameter.§§§

For the sake of clarity, Fig. 9 does not show the trajectories going inside the spheroid, letting Earth and the spheroids appear in the picture. This observation opens a new characterization possibility for the trajectories generated starting from a given (a, C_J) pair. Figure 11 shows a complete classification of the spheroid-phased trajectories.

In particular, based on whether the trajectory is entering or exiting the spheroid, it can be considered either *ingoing* or *outgoing*. This classification follows the simple dot product between the Earth-centric position and velocity vectors $\boldsymbol{r}_{\mathrm{EC}}$ and $\boldsymbol{v}_{\mathrm{EC}}$: ingoing trajectories are characterized by $\boldsymbol{r}_{\mathrm{EC}} \cdot \boldsymbol{v}_{\mathrm{EC}} < 0$, whereas outgoing trajectories feature $\boldsymbol{r}_{\mathrm{EC}} \cdot \boldsymbol{v}_{\mathrm{EC}} > 0$. Tangent trajectories are found with $\boldsymbol{r}_{\mathrm{EC}} \cdot \boldsymbol{v}_{\mathrm{EC}} = 0$, and are neither ingoing nor outgoing. This criterion is a good approximation for spheroids with small eccentricity, and a general and more refined version would replace the direction $\boldsymbol{r}_{\mathrm{EC}}$ with the local perpendicular direction to the spheroid surface. Additionally, based on the true anomaly value, a trajectory can be *inbound* or *outbound*: inbound trajectories are phased so that they are moving from the outer toward the inner solar system with respect to Earth at the time of the encounter, characterized by true anomaly values in the ranges $-\pi < f < 0$ or $\pi < f < 2\pi$. Differently, outbound encounters happen when the trajectory phasing results in a movement from the inner toward the outer the solar system with respect to Earth, characterized by true anomaly values in the ranges $0 < f < \pi$ or $-2\pi < f < -\pi$. The values $f = 0$ and $f = \pi$ correspond to the limit pericenter and apocenter cases, which are neither inbound nor outbound.

§§§In the nonplanar case, a link between the orbital parameters and the spheroid angle θ can also be established through the corresponding spherical trigonometry involving the angles Ω_{rot}, ω, and f. Additionally, all four solutions arising by the $\Omega_{\pm}$ and the $f_{1,2}$ would need to be considered.

C. Keyhole Maps and Generalized Orbital Resonances

Having extended the encounter definition and characterization, this section tries to study the effects of flybys in the extended sense, including shallow interactions and using the CR3BP, focusing on the planar Sun–Earth problem. In particular, new insight on impacts that nominally lie outside the traditional orbital resonances is sought.

In the planar case, the encounter phasing range can be described by sampling secant and tangent trajectories to the $\gamma = 100$ Jacobian spheroid through the angle θ, as presented in Sec. IV.B. For a given Jacobi constant and SMA pair (C_J, a), choosing the angle θ fixes the remaining degree of freedom to completely map the feasible encounter set. Similarly to what presented in Fig. 9, for 100 evenly spaced SMA values within the interval between the 3∶2 and the 1∶2 resonances, a grid of 200 evenly spaced points on the spheroid angle θ is generated, all with the same Jacobi constant $C_J = 2.95$. Then, the trajectory set is first filtered for nonphysical cases (e.g., unreachable points on the spheroid for the given $[C_J, a]$ pair) and split according to the trajectory topology of Fig. 11. The first distinction between ingoing and outgoing trajectories determines the dynamic model used in the study: ingoing trajectories are propagated up to the spheroid exit (unless an impact is detected), whereas outgoing orbits are propagated forward in time for 11 years, or until a new entrance in the $\gamma = 100$ Earth's spheroid is detected.

The ingoing family is split into inbound and outbound, and the propagated trajectories are used to train two simple surrogate models that replace the full CR3BP propagations, yielding a model of impact probability density as a function of Jacobi constant, SMA, and spheroid angle θ, according to three steps. First, the spheroid angle θ^* associated with the minimum altitude encounter is found for each subfamily and each value of SMA. Secondly, the θ^* values are used to train a cubic polynomial regression, that predicts the spheroid angle of maximum flyby depth as function of the SMA, for each subfamily: Fig. 12 represents the maximum encounter depth reached by ingoing trajectories on the color scale, for each pair of SMA (on the x axis) and the entrance spheroid angle θ (on the y axis). The reason why the two subcharts take this peculiar shape is twofold: on the one hand, it arises from the separation of inbound and outbound families; on the other, it is also connected to the limited range of admissible θ for extremal SMA values, as explained in Sec. IV.B. Finally, a standard deviation value equal to the spheroid angle discretization step (0.01π, for the 200 angle samples of this case) is introduced on the modeled θ^*. In this application the choice of this value is entirely arbitrary, and only connected to the following conservative consideration: if an impact is not detected for the considered θ grid, it must be found within the interval surrounding the sampled θ of maximum encounter depth. A possible refinement of this approach would involve the backward mapping of Earth's radius on the spheroid surface for the given C_J values, although beyond the exploration scope of this work. The model represents the mean spheroid angle about which an impact is most likely to be found. Figure 13 samples a few SMA values and shows the associated probability density functions, whereas Fig. 14 shows the full surrogate model. The choice of the cubic regression function is associated with the observed depth map in Fig. 12. For different values of the Jacobi constant, the high impact probability regions may be distributed differently: in particular, cases with $C_J > 3$ would feature the presence of zero-velocity surfaces and of relatively slow encounters, resulting in an impact probability

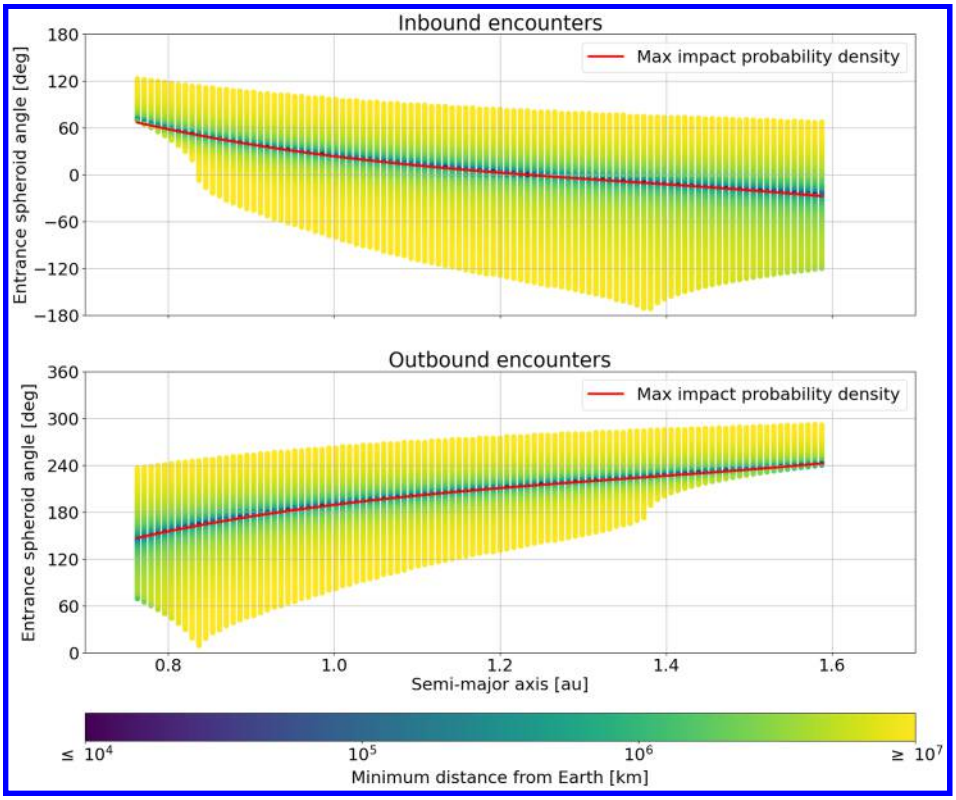

Fig. 12 Maximum encounter depth used as high impact probability metric.

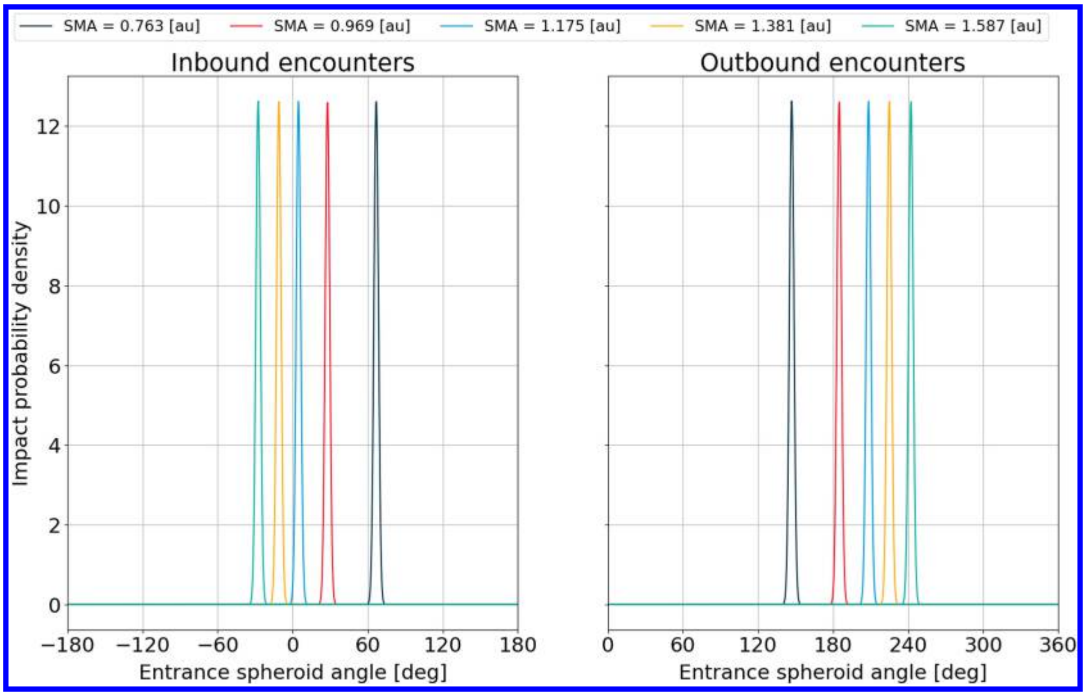

Fig. 13 Sampled surrogate model of impact probability density function.

distribution on the spheroid surface that may require more sophisticated models. In any case, given the considerations made in Sec. IV.B about the uniquely defined orbits at the spheroid boundary, C_J-dependent impact probability surrogate models should still cover the full hazardous encounter range, including slow and shallow ones, provided that the chosen model remains accurate enough.

The outgoing family results in propagated trajectories that either end at the end of the integration span or that experience a new spheroid entrance. For the latter case, the entrance spheroid angle $\tilde{\theta}$ is computed, together with the true anomaly $\tilde{f}$ at the end of the simulation, to detect whether the entrance is happening with inbound or outbound nature. Trajectories with inbound exit resulting in an inbound entrance (or alternatively, outbound exit to outbound entrance) would resemble full resonant returns, i.e., they would be macroscopically similar to the traditional definition by [10]. However, differences can be found in the trajectory phasing, as the zero-radius SOI approximation of [10] with instantaneous deflection of the heliocentric velocity only models a single perfectly phased encounter. On the other hand, considering a finitely sized spheroid and including three-body effects results in a phase range that

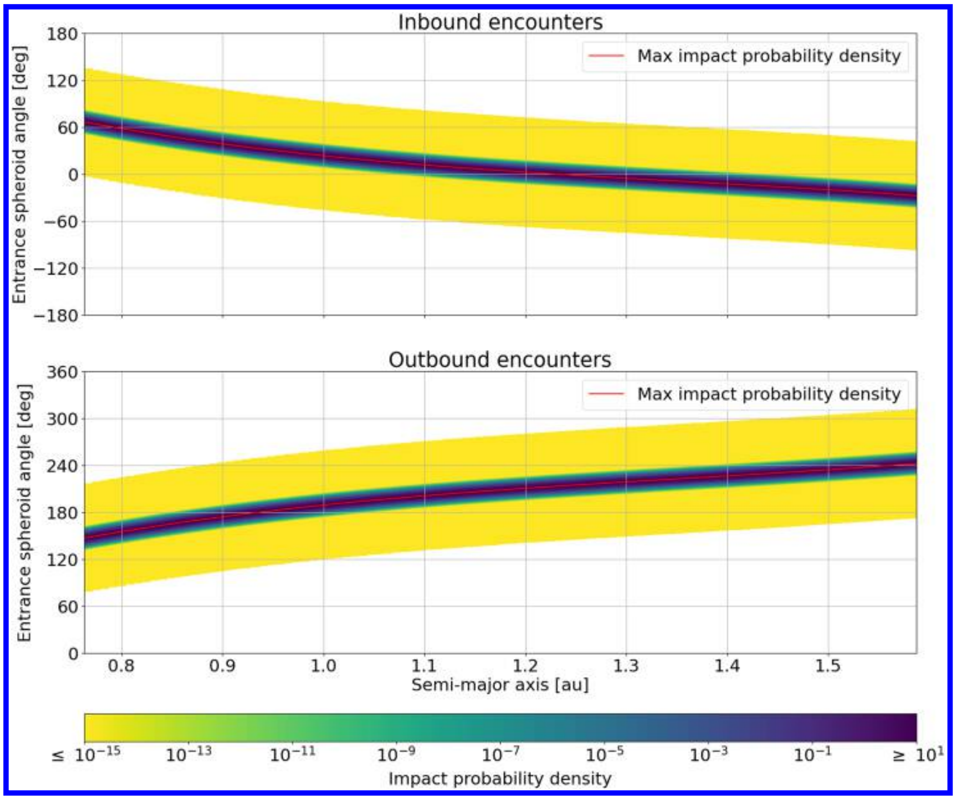

Fig. 14 Overall surrogate model of impact probability density function.

characterizes the encounter, for trajectories that are close to a traditional resonance according to [10] from an heliocentric perspective. Additionally, three-body effects may result in nonperfectly phased encounters (with "perfect phasing" associated to the two-body theory of resonant returns [10]) that can actually be the most hazardous ones. Describing a different type of return instead, trajectories with a switch in the subfamily from the spheroid exit to the next spheroid entrance would look like pseudo-resonant returns, as the next encounter would happen in a position on the heliocentric orbit much different from the one at the previous spheroid exit.

Figure 15 represents the trajectories of the outgoing family with dots, plotting the pair SMA a (on the x axis) and spheroid angle θ

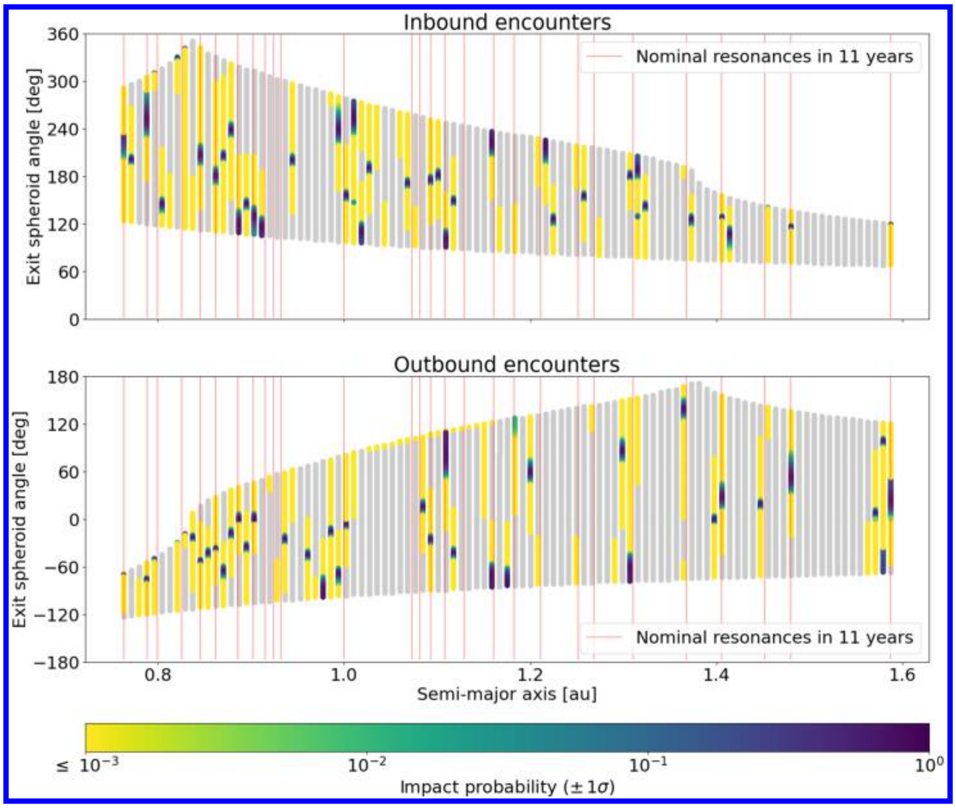

Fig. 15 Sun–Earth keyhole map up to one encounter and 11-year time span.

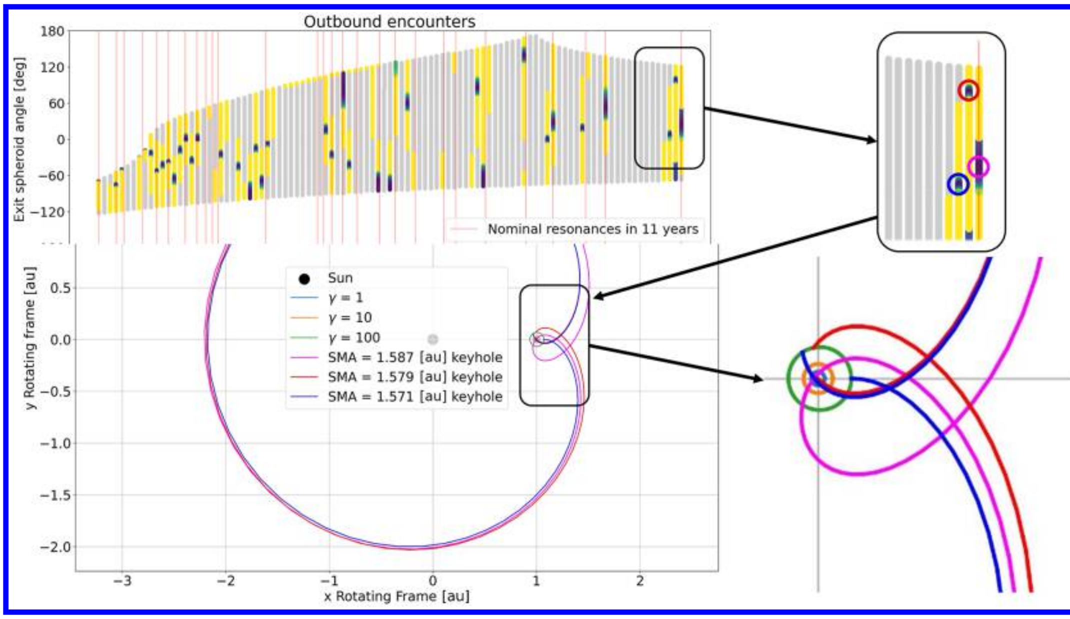

Fig. 16 Keyhole impacting trajectory prediction examples.

(on the y axis) and splitting the inbound (bottom) and outbound (top) subfamilies for the $C_J = 2.95$ case. The predicted impact probability[¶¶¶] associated with each outgoing initial condition is given in the color scale, from low (yellow) to high (blue). Outgoing trajectories that do not result in a new spheroid entrance within the analyzed time span are marked in gray. Each subplot in Fig. 15 is a *Keyhole map*: Keyholes become clearly visible as the regions of the Keyhole map that tend toward the dark blue color. The light red lines represent the nominally resonant SMA values in the 11-year time span according to [10] and provide a useful reference for the keyhole identification: since many of the predicted keyholes appear outside a line of nominal resonance, the proposed impact probability mapping strategy has successfully extended the analysis to nominally off-resonant trajectories.

The Keyhole map in Fig. 15 is constructed by evaluating the surrogate model for the impact probability at the immediate next spheroid entrance, after propagating the trajectories in the two-body problem; in other words, while the Keyhole map has the *exit* spheroid angle θ on the y axis, the *entrance* spheroid angle at the end of the propagation (i.e., at the next spheroid encounter) is used for the impact probability computation with the ingoing surrogate model. Additionally, the surrogate model to be evaluated (inbound vs outbound) is chosen according to the true anomaly at the spheroid entrance for each propagated trajectory. Essentially, the surrogate model is what provides the color to each dot in the Keyhole map, allowing regions of high impact probability to be highlighted. Similarly to what already said for Fig. 12, the peculiar shape of the Keyhole map is due to the chosen value of the Jacobi constant. Specific SMAs are physically prevented from featuring some inbound or outbound conditions because of the constraint in the eccentricity value that results in a threshold of the spheroid angle that certain trajectories can reach. Moreover, only the (a, θ) pairs associated with outgoing trajectories mapped at the next encounter appear in the Keyhole map.

Figure 16 proposes a validation of the Keyhole map approach. The samples at the center of each of the three Keyholes, among the ones already available from the generation of the Keyhole map, are selected and propagated following a two-body heliocentric model up to the spheroid threshold. Here, the propagation switches to the CR3BP. The propagated trajectories are shown in corresponding colors to the highlighted keyholes, i.e., in blue, red, and magenta. While the blue trajectory is supposed to be in nominal resonance with Earth according to [10], as it can be seen by its keyhole being superposed to the red vertical line in Figs. 15 and 16, the propagation result is not an impact, but rather a very deep flyby. This may be explained by the nonperfect phasing, which leads to a still dangerous encounter, although not colliding. Similarly, the magenta trajectory also experiences a low-altitude encounter, although not being in strict resonance with Earth. Finally, the red trajectory ends its propagation with an Earth impact, despite being nominally out of the nominal resonance condition of [10]. In this case, the encounter phasing perfectly compensates the deviation from the nominally nonresonant orbital period, leading to a subsequent collision that could not be predicted using two-body approaches.

The results shown for the Keyhole map validation in Fig. 16, in particular the blue and magenta trajectories not impacting Earth, do not represent an incomplete validation. Rather, the Keyhole map is a statistical graphical tool that has the sole purpose of highlighting regions in the SMA and phasing space that are intrinsically associated with high impact probability levels. In fact, all the trajectories propagated in Fig. 16 experience a very low-altitude encounter, in the order of $10^3 - 10^4$ km: this proves the success of the Keyhole map in this predictions. The map suggests that impacts are indeed located around those regions, even in nominally off-resonant cases. The Keyhole map can support the analysis of hazardous trajectories; the recommended use superposes an outgoing probability distribution, given in terms of SMA and exit spheroid angle, for the computation of impact probabilities corresponding to regions in the Keyhole map that are "wet" by real uncertainty distributions.

V. Conclusions

Jacobian spheroids provide a robust alternative to the definition of SOI, even coming with an analytical solution. Validating this concept on systems with higher mass ratios remains an open point that could either confirm the suitability for Sun–planet-like systems only or even open new research pathways related to the three-body dynamics. Nonetheless, the generic characterization based on the local Lyapunov exponents of the error made by the respective Keplerian approximations remains valid, as well as its link to the local curvature of the gravitational potential. The main flexibility allowed by the γ parameter on the choice of the spheroid threshold lies in its connection with the local Keplerian approximation error. Despite no assumption has been made on the encounter velocity in the proposed Jacobian-based analysis, the mathematical results confirm that the encounter velocity should not play a role in determining which model is locally best suited. Rather, it does play a relevant role, directly

[¶¶¶]From the impact probability measure of Figs. 13 and 14, the computed impact probability is the cumulative probability in the $\pm 1\sigma$ interval around the resulting entrance spheroid angle θ at the next encounter.

ruling the time spent in the different domain regions. Possible future developments should explore this aspect in conjunction with a dynamic choice of γ, attempting to account for higher-ranged encounters for slower trajectories.

The Keyhole map has been computed for planar and single encounter cases only. While studying multiple and inclined encounters completes the theory, this may not be a true limitation for PP/SDM, where the trajectories to be analyzed approximately remain on the planet's orbital plane. The accuracy of the Keyhole map strongly depends on the choices made for the encounter's surrogate model and the complexity of each planetary environment: the γ parameterization ensures that the effects of other planets are statistically irrelevant inside the chosen Jacobian spheroid; whether and how much other internal effects influence the predicted keyholes needs, however, to be assessed. This approach has the potential to avoid large Monte Carlo–based strategies altogether for the computation of impact probabilities in PP and SDM analysis. The already accurate keyhole detection capabilities justify expanding the concept, aiming at including more cases and scenarios. First of all, a chaining strategy should be addressed to "collapse" the map of different encounters, possibly with multiple bodies as well, into a single one, completely representing the impact probability domain in a single graphical tool. Then, the computation of the overall impact probability could be remarkably simplified: all it would take is the superposition of the given uncertainty dispersion over the initial map as a multidimensional probability density function, whose surface integral would finally give the global impact probability.

Acknowledgments

This research has received funding from the European Research Council (ERC) under the European Union's Horizon 2020 research and innovation program as part of the GREEN SPECIES project (Grant Agreement No. 101089265), and from the European Space Agency (ESA) through the Open Space Innovation Platform (OSIP) cofunded research project "Robust Trajectory Design Accounting for Generic Evolving Uncertainties", Contract No. 4000135476/21/NL/GLC/my. This research was supported by grants from NVIDIA® and utilized the NVIDIA RTX A6000 graphics card, awarded by NVIDIA®'s Applied Research Accelerator Programme to the project "GPU-Accelerated Algorithms for Orbital Uncertainty Simulation Applications."

References

[1] "Voyager Missions Webpage," https://voyager.jpl.nasa.gov/ [retrieved Aug. 2023].
[2] "Cassini-Huygens Missions Webpage," https://solarsystem.nasa.gov/missions/cassini/overview/ [retrieved Aug. 2023].
[3] "Bepi-Colombo Missions Webpage," https://www.esa.int/Science_Exploration/Space_Science/BepiColombo [retrieved Aug. 2023].
[4] "Solar Orbiter Definition Study Report (Red Book)," European Space Agency (ESA), July 2011, https://sci.esa.int/s/w7yO4P8.
[5] "Jupiter ICy Moons Explorer Exploring the Emergence of Habitable Worlds Around Gas Giants. Definition Study Report," European Space Agency (ESA) TR 1.0, 2014, https://sci.esa.int/web/juice/-/54994-juice-definition-study-report.
[6] COSPAR—Committee on Space Research, "COSPAR Policy on Planetary Protection," *Space Research Today*, Vol. 208, Aug. 2020, pp. 10–22, https://www.sciencedirect.com/science/article/pii/S1752929820300372.
https://doi.org/10.1016/j.srt.2020.07.009
[7] Kminek, G., "ESA Planetary Protection Requirements," European Space Agency TR ESSB-ST-U-001, 2012.
[8] Armellin, R., Di Lizia, P., Bernelli-Zazzera, F., and Berz, M., "Asteroid Close Encounters Characterization Using Differential Algebra: The Case of Apophis," *Celestial Mechanics and Dynamical Astronomy*, Vol. 107, No. 4, 2010, pp. 451–470.
https://doi.org/10.1007/s10569-010-9283-5
[9] Valsecchi, G. B., Froeschlé, C., and Gonczi, R., "Modelling Close Encounters with Öpik's Theory," *Planetary and Space Science*, Vol. 45, No. 12, 1997, pp. 1561–1574, https://www.sciencedirect.com/science/article/pii/S003206339700072X.
[10] Valsecchi, G. B., Milani, A., Gronchi, G. F., and Chesley, S. R., "Resonant Returns to Close Approaches: Analytical Theory," *Astronomy & Astrophysics*, Vol. 408, No. 3, 2003, pp. 1179–1196.
https://doi.org/10.1051/0004-6361:20031039
[11] Valsecchi, G. B., *Geometric Conditions for Quasi-Collisions in Öpik's Theory*, Springer, Berlin, 2006, pp. 145–158.
https://doi.org/10.1007/3-540-32455-0_6
[12] Valsecchi, G. B., Alessi, E. M., and Rossi, A., "An Analytical Solution for the Swing-By Problem," *Celestial Mechanics and Dynamical Astronomy*, Vol. 123, No. 2, 2015, pp. 151–166.
https://doi.org/10.1007/s10569-015-9631-6
[13] Milani, A., Chesley, S. R., Chodas, P. W., and Valsecchi, G. B., "Asteroid Close Approaches: Analysis and Potential Impact Detection," *Asteroids III*, Univ. of Arizona Press, Tucson, Arizona, 2002, pp. 55–69.
https://doi.org/10.2307/j.ctv1v7zdn4
[14] Opik, E. J., *Interplanetary Encounters: Close-Range Gravitational Interactions*, Vol. 2, Amsterdam, 1976.
[15] Milani, A., "The Asteroid Identification Problem: I. Recovery of Lost Asteroids," *Icarus*, Vol. 137, No. 2, 1999, pp. 269–292.
https://doi.org/10.1006/icar.1999.6045
[16] Milani, A., Sansaturio, M. E., Tommei, G., Arratia, O., and Chesley, S. R., "Multiple Solutions for Asteroid Orbits: Computational Procedure and Applications," *Astronomy & Astrophysics*, Vol. 431, No. 2, 2005, pp. 729–746.
https://doi.org/10.1051/0004-6361:20041737
[17] Milani, A., Chesley, S. R., Sansaturio, M. E., Tommei, G., and Valsecchi, G. B., "Nonlinear Impact Monitoring: Line of Variation Searches for Impactors," *Icarus*, Vol. 173, No. 2, 2005, pp. 362–384.
https://doi.org/10.1016/j.icarus.2004.09.002
[18] Farnocchia, D., Chesley, S. R., Milani, A., Gronchi, G. F., and Chodas, P. W., "Orbits, Long-Term Predictions, Impact Monitoring," *Asteroids IV*, Univ. of Arizona Press, Tucson, Arizona, 2015, pp. 815–834.
https://doi.org/10.2458/azu_uapress_9780816532131
[19] Boutonnet, A., and Rocchi, A., "Taxonomy of Earth Impacting Trajectories: the Case of JUICE Launcher Upper Stage," *AIAA SciTech 2022 Forum*, AIAA Paper 2022-2460, 2022.
https://doi.org/10.2514/6.2022-2460
[20] Wallace, M., "A Massively Parallel Bayesian Approach to Planetary Protection Trajectory Analysis and Design," *Proceedings of the 2015 AAS/AIAA Astrodynamics Specialist Conference*, AAS Paper 15-535, 2015, https://trs.jpl.nasa.gov/handle/2014/45859.
[21] Geda, M., Noomen, R., and Renk, F., "Massive Parallelization of Trajectory Propagations Using GPUs," Master's Thesis, Delft Univ. of Technology, Delft, The Netherlands, 2019, http://resolver.tudelft.nl/uuid:1db3f2d1-c2bb-4188-bd1e-dac67bfd9dab.
[22] Romano, M., Losacco, M., Colombo, C., and Di Lizia, P., "Impact Probability Computation of Near-Earth Objects Using Monte Carlo Line Sampling and Subset Simulation," *Celestial Mechanics and Dynamical Astronomy*, Vol. 132, No. 8, 2020, p. 42.
https://doi.org/10.1007/s10569-020-09981-5
[23] Masat, A., Romano, M., and Colombo, C., "Kustaanheimo-Stiefel Variables for Planetary Protection Compliance Analysis," *Journal of Guidance, Control, and Dynamics*, Vol. 45, No. 7, 2022, pp. 1286–1298.
https://doi.org/10.2514/1.G006255
[24] Russell, R. P., "Survey of Spacecraft Trajectory Design in Strongly Perturbed Environments," *Journal of Guidance, Control, and Dynamics*, Vol. 35, No. 3, 2012, pp. 705–720.
https://doi.org/10.2514/1.56813
[25] Campagnola, S., and Russell, R. P., "Endgame Problem Part 2: Multibody Technique and the Tisserand-Poincare Graph," *Journal of Guidance, Control, and Dynamics*, Vol. 33, No. 2, 2010, pp. 476–486.
https://doi.org/10.2514/1.44290
[26] Malyshkin, L., and Tremaine, S., "The Keplerian Map for the Planar Restricted Three-Body Problem as a Model of Comet Evolution," *Icarus*, Vol. 141, No. 2, 1999, pp. 341–353.
https://doi.org/10.1006/icar.1999.6174
[27] Grover, P., and Ross, S., "Designing Trajectories in a Planet-Moon Environment Using the Controlled Keplerian Map," *Journal of Guidance, Control, and Dynamics*, Vol. 32, No. 2, 2009, pp. 437–444.
https://doi.org/10.2514/1.38320
[28] Ross, S. D., and Scheeres, D. J., "Multiple Gravity Assists, Capture, and Escape in the Restricted Three-Body Problem," *SIAM Journal on Applied Dynamical Systems*, Vol. 6, No. 3, 2007, pp. 576–596.
https://doi.org/10.1137/060663374
[29] Cavallari, I., Grassi, C., Gronchi, G. F., Baù, G., and Valsecchi, G. B., "A Dynamical Definition of the Sphere of Influence of the Earth," *Communications in Nonlinear Science and Numerical Simulation*, Vol. 119, May 2023, Paper 107091.
https://doi.org/10.1016/j.cnsns.2023.107091

[30] Amato, D., Baù, G., and Bombardelli, C., "Accurate Orbit Propagation in the Presence of Planetary Close Encounters," *Monthly Notices of the Royal Astronomical Society*, Vol. 470, No. 2, 2017, pp. 2079–2099. https://doi.org/10.1093/mnras/stx1254

[31] Romano, M., "Orbit Propagation and Uncertainty Modelling for Planetary Protection Compliance Verification," Ph.D. Thesis, Politecnico di Milano, Milan, Feb. 2020. https://doi.org/10.13140/RG.2.2.19692.80001

[32] Debatin, F., Tilgner, A., and Hechler, F., "Fast Numerical Integration of Interplanetary Orbits," Vol. 255, ESA Special Publ., European Space Operations Centre (ESA/ESOC), Darmstdt, Germany, 1986, pp. 329–333.

[33] Negri, R. B., and Prado, A. F. B. A., "Shallow Encounters' Impact on Asteroid Deflection Prediction and Implications on Trajectory Design," *Journal of Guidance, Control, and Dynamics*, Vol. 47, No. 7, 2024, pp. 1–18. https://doi.org/10.2514/1.G007890

[34] Masat, A., Colombo, C., and Boutonnet, A., "Flyby Dynamical Characterisation with Jacobian Eigenvalues," *5th International Workshop on Key Topics in Orbit Propagation Applied to SSA*, Politecnico di Milano, 2022, https://hdl.handle.net/11311/1222116.

[35] McClain, W., and Vallado, D., *Fundamentals of Astrodynamics and Applications*, Space Technology Library, Springer, Dordrecht, The Netherlands, 2001, https://books.google.it/books?id=PJLlWzMBKjkC.

[36] "GODOT Documentation," https://godot.io.esa.int/godotpy/ [retrieved May 2024].

[37] "CUDAjectory Documentation," May 2024, https://ad.space-codev.org/cudajectory/ [retrieved May 2024].

[38] Masat, A., Colombo, C., and Boutonnet, A., "GPU-Based Augmented Trajectory Propagation: Orbital Regularization Interface and NVIDIA CUDA Tensor Core Performance," *9th ICATT - International Conference on Astrodynamics Tools and Techniques*, European Space Agency, Paper 199, 2023. https://doi.org/10.5270/esa-gnc-icatt-2023-199

[39] Carusi, A., Valsechi, G. B., and Greenberg, R., "Planetary Close Encounters: Geometry of Approach and Post-Encounter Orbital Parameters," *Celestial Mechanics and Dynamical Astronomy*, Vol. 49, No. 2, 1990, pp. 111–131. https://doi.org/10.1007/BF00050709

[40] Quarteroni, A., Sacco, R., and Saleri, F., *Numerical Mathematics Texts in Applied Mathematics*, Springer, Berlin, 2007. https://doi.org/10.1007/b98885

[41] Silvester, J. R., "Determinants of Block Matrices," *Mathematical Gazette*, Vol. 84, No. 501, Nov. 2000, pp. 460–467. https://doi.org/10.2307/3620776

[42] Abarbanel, H. D. I., Brown, R., and Kennel, M. B., "Local Lyapunov Exponents Computed from Observed Data," *Journal of Nonlinear Science*, Vol. 2, No. 3, 1992, pp. 343–365. https://doi.org/10.1007/BF01208929

[43] Cencini, M., Cecconi, F., and Vulpiani, A., *Chaos*, World Scientific, Singapore, 2009. https://doi.org/10.1142/7351

[44] Campiti, G., Masat, A., and Colombo, C., "Resonant Flybys in the B-Plane: Extension of the Theory to Elliptical Planetary Orbits and Dynamic Programming Application," Master's Thesis, Politecnico di Milano, Milan, 2021, http://hdl.handle.net/10589/179968.

M. Macdonald
Associate Editor